Applied Thermal Engineering 228 (2023) 120525

Contents lists available at ScienceDirect

Applied Thermal Engineering

journal homepage: www.elsevier.com/locate/apthermeng

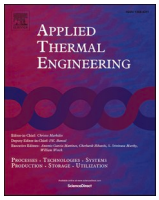

Research Paper

Experimental and analytical investigation of applying an asymmetric plate heat exchanger as an evaporator in a thermally driven adsorption appliance

Makram Mikhaeil [a,b], Sebastian Nowak [a], Valeria Palomba [c], Andrea Frazzica [c], Matthias Gaderer [d], Belal Dawoud [a,*]

[a] East Bavarian Technical University of Applied Sciences (OTH Regensburg), Faculty of mechanical Engineering, Laboratory of Sorption Processes, Galgenberg street 30, 93053 Regensburg, Germany
[b] Menofia University, Faculty of Engineering, Mechanical Power Engineering Department, Shebin-El-Kom, Egypt
[c] CNR – ITAE - Istituto di Tecnologie Avanzate per l'Energia "Nicola Giordano", Salita S. Lucia sopra Contesse 5, Messina 98126, Italy
[d] TUM Campus Straubing for Biotechnology and Sustainability, Chair Regenerative Energy Systems, Technical University of Munich, Schulgasse 16, 94315 Straubing, Germany

ARTICLE INFO

Keywords:
Adsorption-evaporation
Evaporator
Plate heat exchanger
Thin film evaporation

ABSTRACT

This communication presents an experimental and analytical study on the evaporation mechanism in a closed-structured asymmetric plate heat exchanger (PHE) employed as a stagnant water evaporator for the application in an adsorption heat transformation appliance. To this aim, an experimental unit is constructed, which comprises two identical PHEs, one acting as an evaporator/condenser and the second, as an adsorber/desorber. Two endoscopes are mounted inside the investigated evaporator to visualize the evaporation mechanism when performing adsorption-evaporation processes under different boundary conditions. It turned out that the evaporation mechanism is a partially covered, thin film evaporation. A heat transfer analysis is performed to evaluate the heat transfer coefficient of the thin film evaporation (h_f) inside the investigated evaporator, resulting in h_f-values between 1330 and 160 [W•m^{-2}•K^{-1}] over the investigated adsorption-evaporation time. Correlating the obtained (h_f) to the film thickness δ and the wetted area A_{wet} results in δ-values between 0.34 and 0.78 [mm] and wetted to total area ratios A_{wet}/A_{total} of 0.78 to 0.16. Besides, an analytical model has been developed and introduced to correlate the overall evaporator heat transfer coefficient with the adsorption potential and the time rate of change of the water uptake.

1. Introduction

Realizing compact, highly efficient, and affordable components for the application in thermally driven adsorption (TDAd) cooling and heating appliances promotes the competitiveness of such environmentally friendly systems against the traditional vapor compression systems. The wide-adoption of TDAd-appliances for cooling and heating purposes is a key measure to enable sustainable cooling and heating, as the driving energy is low-grade heat [1,2], which is abundantly available from solar and waste heat sources. In addition, adsorption systems enable the use of water as refrigerant, which is natural, safe and has neither a global warming potential (GWP) nor an ozone depletion potential (ODP). The research in the field of the TDAd-systems deals mostly with developing new adsorbent-adsorbate working pairs [3–9], investigating the adsorption and desorption kinetics of adsorbent-adsorbate pairs [10–13], investigating the performance of adsorber heat exchangers [2,14–18] and optimizing the thermal management of adsorption systems [19,20]. Indeed, there are many research communications dealing with the evaporator/condenser heat exchanger (HEx) applied generally in the cooling and heating appliances. However, there is a noticeable lack in the research dealing with the application of plate-type heat exchangers to act as evaporator/condenser in adsorption appliances. Applying plate heat exchangers (PHEx) instead of fin-and-tube or falling film ones could result in highly compact and efficient adsorption systems. The application of asymmetric plate heat exchangers (APHEx), which are characterized by heat transfer between two separated domains of unequal volume, to act as evaporator/condenser in the adsorption systems could come with the advantage of realizing high heat transfer coefficients and low-pressure drops leading to a significant enhancement in the heat and mass transfer rates [21].

Some studies addressed the application of plate heat exchangers for

* Corresponding author.
E-mail address: belal.dawoud@oth-regensburg.de (B. Dawoud).

https://doi.org/10.1016/j.applthermaleng.2023.120525
Received 1 September 2022; Received in revised form 19 October 2022; Accepted 6 March 2023
Available online 11 April 2023
1359-4311/© 2023 The Author(s). Published by Elsevier Ltd. This is an open access article under the CC BY-NC-ND license (http://creativecommons.org/licenses/by-nc-nd/4.0/).

Nomenclature

A	Adsorption potential or Dubinin-Polanyi's potential, [J•kg^{-1}]
A_{total}	total area of the plates surface, [m^2]
A_{wet}	Wetted area of the plates surface [m^2]
c_p	specific heat capacity, [J•kg^{-1}•K^{-1}]
d_h	hydraulic diameter, [m]
H	heat transfer coefficient, [W•m^{-2}•K^{-1}]
h_{fg}	latent heat of vaporization, [J•kg^{-1}]
K	thermal conductivity, [W•m^{-1}•K^{-1}]
L_{plate}	plate (wall) thickness, [m]
M	mass, kg
Nu	Nusselt number
P	Pressure, [Pa]
Pr	Prandtl number
$\dot{Q}$	thermal power, [W]
R	thermal resistance, [K•W^{-1}]
Re	Reynolds number
t	time, [s]
T	temperature, [°C]
U	overall heat transfer coefficient, [W•m^{-2}•K^{-1}]
V	volume, [m^3]
$\dot{V}$	volume flow rate, [m^3•s^{-1}]
w	water uptake, [kg•kg^{-1}]

Greek letters

δ	film thickness, [m]
ρ	density, [kg•m^{-3}]
Δ	Measurement uncertainty, -

Subscripts

0	Initial
ads	Adsorbent
cond	Condenser
corr	Correlated
evap	Evaporator
in	Inlet
l	Liquid
min	Minimum
out	Outlet
ref	Refrigerant
sorb	Sorbent
f	thin film

Abbreviations

APHEx	asymmetric plate heat exchanger
HEx	heat exchanger
HTC	heat transfer coefficient
HTF	heat transfer fluid
LSP	Laboratory of Sorption Processes
LTJ	large temperature jump
PHEx	plate heat exchanger

evaporation processes. Most of them dealt with refrigerants like R134a, R22, R290 R245fa or ammonia [22–26]. It has been found that the evaporation heat transfer coefficient (HTC) increases with increasing the refrigerant vapour quality and mass flux [22–24] as well as with increasing the heat flux and the refrigerant saturation temperature [24]. Some studies dealt, however, with the evaporation of water as a refrigerant. In [27], the flow boiling heat transfer in a vertical-chevron-type PHEx at low mass fluxes ($200 < Re < 600$) and under atmospheric conditions is investigated. It has been found that the HTC depends on the mean vapour quality and the mass flux.

The evaporation of water under sub-atmospheric conditions has also been investigated in some studies. For instance, in [28,29] water evaporation in a fin-and-tube heat exchanger, where pool boiling regime has been realized, has been investigated. In [30,31], water evaporation on the surface of tubes with microscopic fin structures and microporous coating layers, which provide a capillary effect and, consequently, enable realizing wetted tube surface with a thin water film, has been investigated. It has been reported that the heat transfer coefficient increases with the evaporation temperature. Besides, it has been recommended to make the filling level of the evaporator heat exchanger as low as possible, but the tube's surface should be kept always wet. The authors in [32,33] studied the water evaporation on a smooth vertical channel, which mimics a plate heat exchanger with smooth plates surface, under typical operating conditions of the LiBr/H_2O sorption chillers. It has been reported in [32] that during the water evaporation in the vertical channel three successive flow regimes were observed with zero measured cooling capacity during the first flow regime, which was characterized by appearance and quick collapse of bubbles at the channel inlet. During the two latter flow regimes, three different areas, upper, middle and lower were identified in the channel. The authors attributed the achieved cooling capacity mainly to the evaporation of the liquid film formed on the upper area of the channel. The authors concluded that the higher the mass flux and thus the thinner the liquid film, the higher also the achieved cooling capacity [32]. Another parameter of influence on the water evaporation in a vertical channel is the filling level. It was concluded in [33] that the HTC and the cooling capacity increase with rising the filling up to a certain critical level. Beyond such a critical level, further increasing the filling level resulted in a rapid decrement in both HTC and the cooling capacity.

In [34], the authors investigated the thin film evaporation mode of water in a partially flooded tube-fin HEx at sub-atmospheric conditions. The major factor of influence on the thin film evaporation has been found to be the mass flow rate of the heat transfer fluid (HTF). Increasing the HTF's mass flow rate increases the flow turbulence and, accordingly, increases the overall heat transfer coefficient of the evaporator heat exchanger.

It can be concluded, that so far, no experimental studies on the application of asymmetric plate heat exchangers acting as evaporator/condenser under the operating conditions of adsorption heat transformation appliances exist in the literature. To the authors' knowledge, most of the research deals with finned circular and flat tube heat exchangers with refrigerants like R134a, R22, R290 R245fa or ammonia, but less with water. Indeed, few research articles addressed the application of vertical plate heat exchangers as evaporator, however, studies investigating the evaporation in a horizontal plate heat exchangers don't exist. This gap shall be filled by the present work, which aims at investigating the application of an asymmetric plate heat exchanger as an evaporator of an adsorption heat transformation appliance. Hereby, two endoscopes are utilized to visualize the evaporation mechanism inside a commercially available asymmetric plate heat exchanger mounted horizontally and tested as a stagnant evaporator against an adsorber heat exchanger under typical operating conditions of an adsorption chiller. Besides, a correlation between the evaporator and the adsorber performances is developed. Furthermore, an analytical model is introduced to describe the identified evaporation mechanism inside the investigated evaporator, and the assumptions made for it are verified using the visualizations obtained from the endoscopes.

2. Experimental setup and test procedure

2.1. Test unit

A pair of identical stainless steel (316 L) PHEs, with the trade name "GL50" [35,36] produced by Alfa Laval©, Sweden, is employed to assemble a test unit for investigating the performance of asymmetric closed-structure PHE acting as evaporator/condenser for the application in adsorption heat transformation processes. Fig. 1.a depicts a schematic of the test unit, while Fig. 1.b shows the 3D-drawing of the assembled components at the Laboratory of Sorption Processes (LSP) of OTH Regensburg. One of the two identical "GL50" PHEs is adapted and employed to act as an adsorber/desorber (upper PHEx in Fig. 1.b), which has been filled with 790 [g] of loose microporous Siogel grains (Oker Chemie, Germany) in the size range of 0.71 to 1.0 [mm]. The other "GL50 "PHE has been employed to act as a horizontally mounted evaporator/condenser heat exchanger (lower PHEx in Fig. 1.b). Each PHE comprises a stack of 20 plates. Table 1 presents the specifications of the "GL50" PHE [36]. The matching between the adsorption/desorption kinetics on small- and full-scale adsorber of the test unit depicted in Fig. 1 can be read elsewhere [37]. In addition, two adsorber sizes; namely 20 and 40 plates, have been investigated against an evaporator-condenser comprising a 20-plate evaporator-condenser and the results have been presented in [38]. Moreover, a comparison between the obtained experimental results on an open-structured PHE acting as an adsorber-desorber [15] and the introduced adsorption unit (Fig. 1) comprising closed-structure PHEs has been reported on in [39].

As illustrated in Fig. 1, both PHEs are connected through two separated pipelines. The connecting pipes allow the water vapour to transfer between the two PHEs. Two vacuum gate-valves (V2.1 and V2.2) of type DN40 are mounted on the pipelines to allow separating/connecting the two PHEs from/to each other. Two pressure transducers ($P1$ and $P2$) are mounted on the pipelines connecting the two PHEs together (see Fig. 1. a) to measure the pressure of the water vapour in each PHE. Finally, two extra vacuum valves (V1.1 and V1.2) are mounted on the pipelines to allow evacuating the two PHEs separately as well as filling in the evaporator/condenser with degassed water under vacuum. In this work, the evaporator/condenser heat exchanger has been filled with 225 [g] of degassed water.

Two different endoscope video cameras (BS-3.9/1m QVGA and BS-350XIPSD, from VOLTCRAFT®) are used for the visualization of the evaporation process inside the investigated evaporator heat exchanger. The main characteristics of the endoscopes are listed in Table 2. The endoscopes are inserted into the evaporator heat exchanger using an electrical vacuum feedthrough (MIL-C-24308) on a KF40 flange (VACOM®), as shown in Fig. 2. The installation positions of the endoscopes inside the evaporator heat exchanger are schematically illustrated Fig. 3, where it can be seen that one endoscope, namely endoscope (1), is positioned inside the fifth refrigerant channel to visualize the evaporation mechanism. Endoscope (2) is positioned in one

Table 1
Geometric parameters of the applied adsorber and evaporator plate heat exchangers.

Parameter	Value
Number of plates	20
Overall dimensions	278 [mm] × 123 [mm] × 83 [mm]
Heat transfer surface per plate	0.0393 [m^2]
Empty weight	3.4 [kg]
Volume refrigerant side	1.5 [L]
Volume HTF side	0.9 [L]
Plate thickness	0.35 [mm]

Table 2
Properties of the used endoscope video cameras.

Parameter	Endoscope (1)	Endoscope (2)
Model	BS-3.9/1m QVGA	BS-350XIPSD
Position	refrigerant channel	manifold
Diameter	3.9 [mm]	8 [mm]
Resolution	320x240	640x480
Focusing	10 [mm] to 50 [mm]	30 [mm] to 60 [mm]
Field of vision	54°	54°

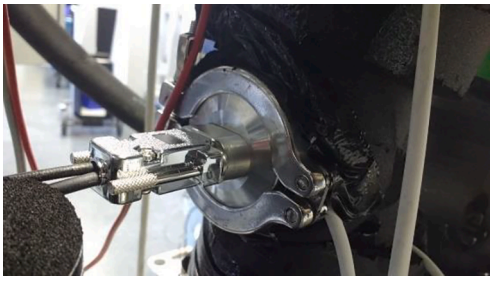

Fig. 2. Vacuum feedthrough of the two endoscope cameras into the test unit.

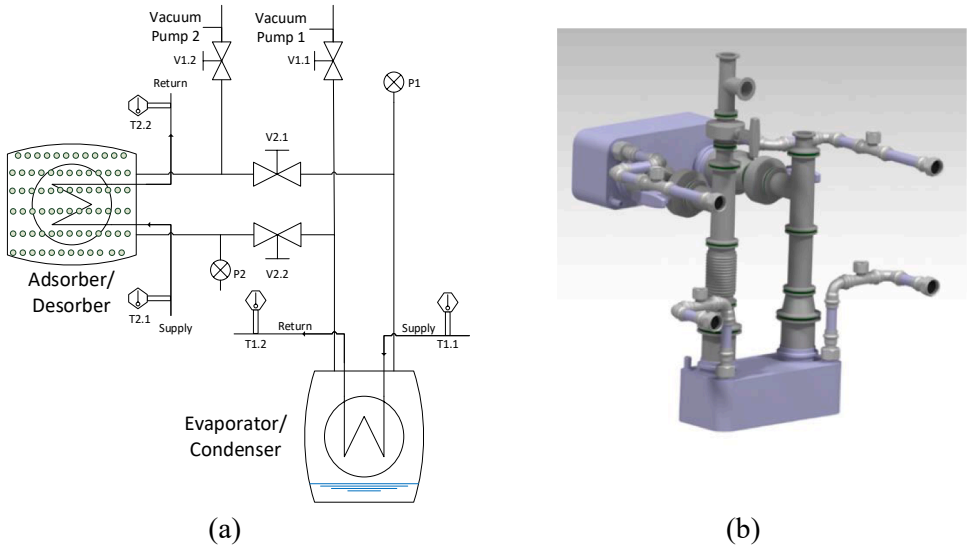

Fig. 1. Layout of the test unit. (a) Schematic layout including the most important sensors and actuators, (b) 3D-drawing of the assembled components.

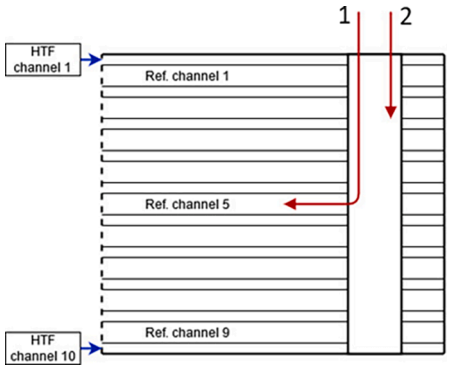

Fig. 3. Schematic drawing for illustrating the position of endoscopes (1) and (2) inside the evaporator heat exchanger.

of the two refrigerant vapour manifolds of the evaporator heat exchanger to observe the bottom of the manifold as well as the inlet of the refrigerant channels interfaced with the vapour manifold.

A Helium leakage test has been carried out to ensure the tightness of the adsorption unit. To prevent undesired local vapour condensation on the inner surface of the connection piping and valves, especially during the condensation-desorption processes, a controlled heating cable is wrapped around them to keep their wall temperature higher than the condensation temperature. The set-up is well insulated to minimize the heat losses. Fig. 4 illustrates the realized test unit at the LSP of OTH-Regensburg, Germany.

A special hydraulic setup, installed in the LSP of OTH-Regensburg, has been utilized for feeding the two PHExs of the test unit, simultaneously with HTFs set at automatically controlled temperatures and flow rates. The hydraulic setup comprises two separated hydraulic circuits, a primary and a secondary circuit. The primary circuit feeds the adsorber/desorber heat exchanger, whereas the secondary-one feeds the evaporator/condenser heat exchanger. The HTF applied in both hydraulic circuits is water. The volumetric flow rate in each circuit is set to 6 [L.min^{-1}] during the investigations carried out in this work. The type and accuracy of the individual sensors applied for measuring the pressure of the adsorbate vapour in both heat exchangers, the inlet and outlet temperatures and flow rate of the HTFs passing through them are listed in Table 3.

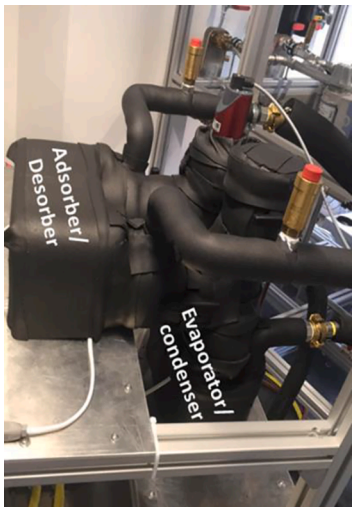

Fig. 4. Realized test unit for investigating the "GL50" PHE as evaporator/condenser at the LSP of OTH-Regensburg, Germany.

Table 3
List of applied sensors and their accuracy [40–43].

Sensor	Accuracy	Measured quantity
Balance KERN type EMB 6000–1	±0.1 [g]	Dry weight of the adsorbent
Pressure transducers PFEIFFER VACUUM type CMR 362	±0.2 % of reading	Vapour pressure inside the testing rig
RTD temperature sensors TMH type Pt100	1/10 DIN class B	HTF temperatures
Flow meters SIEMENS type Sitrans F M MAG 6000	±0.2 % ± 1 [mm/s]	Volume flow rate of the HTF

2.2. Test conditions and experimental procedure

Throughout the course of this work, the adsorption-evaporation processes have been conducted following the Large Temperature Jump (LTJ) technique under different operating conditions of a real adsorption chiller. Fig. 5 presents the ideal adsorption chiller process (in black) versus those taking place in a real adsorption chiller (in red). As the evaporator-condenser heat exchanger is not of infinite size, the pressure can't be kept constant. At the beginning of each process, the adsorption or desorption sucks or drives out more water vapour than that producible by the evaporator or condensable by the condenser. As the system is an adsorption unit represented thermodynamically as a closed system, the pressure shall decrease/increase at the beginning of the adsorption/desorption process, respectively, the case of the red lines 4–1 for adsorption and 2–3 for desorption in Fig. 5. Approaching the final equilibrium state, the rate of adsorption/desorption decreases, so that the size of the evaporator/condenser becomes big enough to retain the initial pressure level according to the inlet temperature into the heat exchanger.

The LTJ adsorption-evaporation processes have been conducted at evaporator temperatures (T_{evap}) of 10 and 15 [°C], condenser (adsorption-end) temperatures ($T_{cond} = T_{ads-end}$) of 30 and 35 [°C] and driving heat source (desorption-end) temperature (T_h) of 90 [°C]. The adsorption-start temperature (ads-start), i.e., the temperature of state 4 (T_4) has been determined using the equilibrium model developed in [44] for water adsorption in Siogel at all defined sets of operating conditions and listed in Table 4. Two selected sets of operating conditions, namely 15/30/90 [°C] and 10/35/90 [°C], have been conducted 3 times to check the repeatability of the measurements.

The test procedure of a LTJ adsorption-evaporation process consists of the following two phases, during which the gate valves (V2.1 and V2.2) connecting the adsorber to the evaporator are kept open:

The preparation phase, which aims at realizing the adsorption start condition. This is done by setting the adsorber heat exchanger to the adsorption start temperature (T_4) and, at the same time, setting the temperature of the evaporator heat exchanger to the required evaporation temperature (T_{evap}). This preparation phase takes 2 h to ensure reaching the equilibrium state 4.

The second phase is the LTJ-quasi-isobaric adsorption phase, in which the temperature of the HTF feeding the adsorber experiences a step-change to the adsorption-end temperature (T_1). The LabVIEW code written to control the whole set-up allows setting the desired end-temperature and realizing it at the inlet of the adsorber heat exchanger in about 2 min after finishing phase one. The adsorption phase is measured over 2 h to ensure reaching the equilibrium condition at the end of the process.

The investigation results of the desorption-condensation processes (2–3 in Fig. 5) along with the identified condensation mechanism, with the help of the mounted endoscopes, are the subject of a separate communication, which is under preparation.

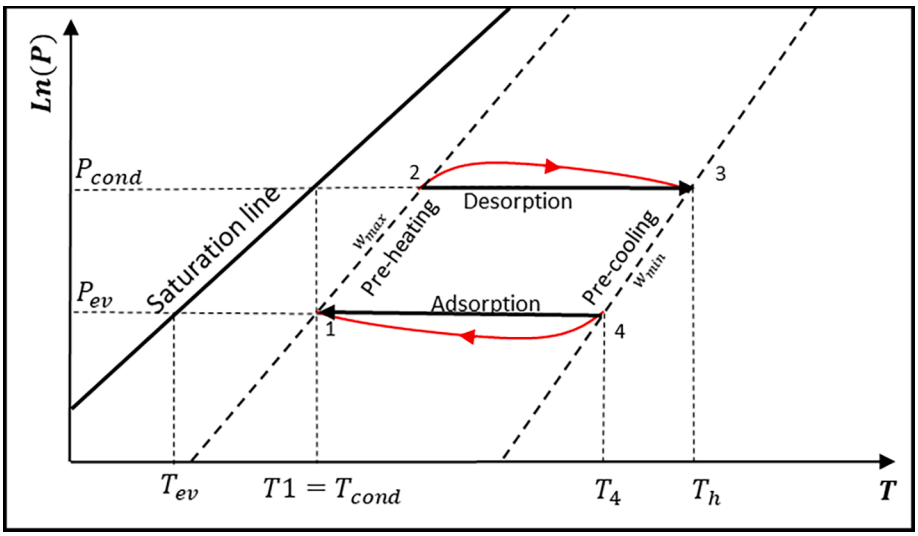

Fig. 5. Schematic representation of both ideal and real adsorption and desorption processes of an adsorption chiller in a Clapeyron diagram.

Table 4
Boundary conditions of the conducted adsorption-evaporation processes.

Process	$T_{evap}/T_{cond}/T_h$ [°C]	$T_{ads-start}$, T_4 [°C]	$T_{ads-end}$ or T_{cond},T_1 [°C]
1	10/30/90	66.1	30.0
2	10/35/90	58.8	35.0
3	15/30/90	70.5	30.0
4	15/35/90	62.4	35.0

2.3. Evaluation of the evaporator performance

A MATLAB® code has been developed to estimate the evaporator power out of the recorded experimental data, the overall and the individual heat transfer coefficients of the investigated evaporator heat exchanger for all conducted adsorption-evaporation processes (see Table 4). The achieved evaporator power has been calculated according to Eq. (1),

$$\dot{Q}_{evap} = \dot{V}_{HTF} \cdot \rho_{HTF} \cdot c_{p,HTF} \cdot \left(T_{HTF,in} - T_{HTF,out}\right) \quad (1)$$

Where $\dot{Q}_{evap}$ [W] is the evaporator power, $\dot{V}_{HTF}$ [$m^3 \bullet s^{-1}$] is the measured volume flow rate of the heat transfer fluid (HTF), ρ_{HTF} [$kg \bullet m^{-3}$] is the density of the HTF, $c_{p,HTF}$ [$J \bullet kg^{-1} \bullet K^{-1}$] is its specific heat capacity and $T_{HTF,in}$ [K] and $T_{HTF,out}$ [K] are the measured inlet and outlet temperature of the HTF. The thermodynamic properties of the HTF (water) have been determined at the mean temperature between the inlet and outlet of the HTF passing through the evaporator heat exchanger using the thermophysical property database *CoolProp*, which is coupled to MATLAB®.

Having calculated the evaporator power, the overall heat transfer coefficient U [$W \bullet m^{-2} \bullet K^{-1}$] in the evaporator can be estimated by the following equation.

$$U = \frac{\dot{Q}_{evap}}{A_{total} LMTD} \quad (2)$$

Where A_{total} [m^2] is the heat transfer area of the evaporator and $LMTD$ [K] is the logarithmic mean temperature difference, which is defined by Eq. (3).

$$LMTD = \frac{T_{HTF,in} - T_{HTF,out}}{ln \frac{T_{HTF,in} - T_{ref}}{T_{HTF,out} - T_{ref}}}. \quad (3)$$

T_{ref} is the saturation temperature of the refrigerant (water) corresponding to the measured vapour pressure inside the evaporator (P_{evap}).

The total thermal resistance of the evaporator heat exchanger can be represented as a series connection of three resistances as shown in Fig. 6. Accordingly, the overall thermal resistance R_{total} [$K \bullet W^{-1}$] can be expressed as:

$$R_{total} = R_{ref} + R_{plate} + R_{HTF} \quad (4)$$

Where R_{ref} [$K \bullet W^{-1}$] is the thermal resistance of the evaporating water from the channel's wall, R_{HTF} [$K \bullet W^{-1}$] is the convective heat transfer resistance between the HTF and the channel's wall and R_{plate} [$K \bullet W^{-1}$] is the conductive thermal resistance through the channel's wall.

Based on the basic heat transfer relationship (Eq. (5)), between the overall heat transfer coefficient and the total thermal resistance, the unknown evaporative heat transfer coefficient on the refrigerant (water) side h_f [$W \bullet m^{-2} \bullet K^{-1}$] can be determined by Eq. (6).

$$UA_{total} = \frac{1}{R_{total}} \quad (5)$$

$$h_f = \left(\frac{1}{U} - \frac{1}{h_{HTF}} - \frac{1}{h_{plate}}\right)^{-1} \quad (6)$$

where the heat transfer coefficient h_{plate} [$W \bullet m^{-2} \bullet K^{-1}$] represents the conduction through the wall (see Eq. (7)) and h_{HTF} [$W \bullet m^{-2} \bullet K^{-1}$] is the convective heat transfer coefficient between the wall and the HTF (cf. Eqs. (8) and (9)).

$$h_{plate} = \frac{k_{plate}}{L_{plate}} \quad (7)$$

Where k_{plate} is the thermal conductivity of the plate, amounts 15

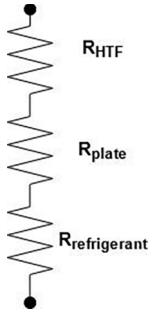

Fig. 6. Thermal resistances of the evaporator HEx.

[W•m^{-1}•K^{-1}] and L_{plate} [m] is the plate thickness, amounts to 0.35 [mm].

The heat transfer coefficient h_{HTF} between the wall and the HTF is determined using the correlation proposed by Gnielinski [45]:

$$Nu = 0.664\ Re_{HTF}^{1/2}\ Pr^{1/3} \tag{8}$$

$$h_{HTF} = 1.5\ Nu\ \frac{k_{HTF}}{d_{h,HTF}} \tag{9}$$

Where Nu is the Nusselt number, Re is the Reynolds number of the HTF and Pr its Prandtl number. k_{HTF}[W.m^{-1}K^{-1}] is the thermal conductivity of the HTF and $d_{h,HTF}$[m] the hydraulic diameter of the HTF channel. $d_{h,HTF}$ is estimated using the 3D drawings of the"GL50″ plates and equals 7.5E-3 [m]. The factor 1.5 is to account for the effect of the dimples on the h_{HTF} [46–48].

2.4. Uncertainty of the measurements

The uncertainty of the overall heat transfer coefficient (ΔU) is calculated by means of the law of error propagation for Eq. (2), leading to the following expression,

$$\Delta U = \sqrt{\left(\frac{\partial U}{\partial \dot{Q}_{evap}}\Delta \dot{Q}_{evap}\right)^2 + \left(\frac{\partial U}{\partial LMTD}\Delta LMTD\right)^2 + \left(\frac{\partial U}{\partial A}\Delta A_{total}\right)^2} \tag{10}$$

With $\Delta \dot{Q}_{evap}$, $\Delta LMTD$ and ΔA_{total} being the uncertainty of the evaporator power, the logarithmic mean temperature difference (LMTD) and the overall heat transfer area, respectively. $\Delta \dot{Q}_{evap}$ and $\Delta LMTD$ are determined by means of the law of error propagation for Eq. (1) and Eq. (3), respectively. ΔA_{total} is estimated based on the uncertainty of the plate dimensions given by the "GL50" PHE's manufacturer [36] and found about ± 1.55 %.

$$\Delta \dot{Q}_{evap} = \sqrt{\left(\frac{\partial \dot{Q}_{evap}}{\partial T_{HTF,in}}\Delta T_{HTF,in}\right)^2 + \left(\frac{\partial \dot{Q}_{evap}}{\partial T_{HTF,out}}\Delta T_{HTF,out}\right)^2 + \left(\frac{\partial \dot{Q}_{evap}}{\partial \dot{V}_{HTF}}\Delta \dot{V}_{HTF}\right)^2} \tag{11}$$

The uncertainty of ρ_{HTF} and $c_{p,HTF}$, i.e., $\Delta\rho_{HTF}$ and $\Delta c_{p,HTF}$ have been neglected.

$$\Delta LMTD = \sqrt{\left(\frac{\partial LMTD}{\partial T_{HTF,in}}\Delta T_{HTF,in}\right)^2 + \left(\frac{\partial LMTD}{\partial T_{HTF,out}}\Delta T_{HTF,out}\right)^2 + \left(\frac{\partial LMTD}{\partial T_{ref}}\Delta T_{ref}\right)^2} \tag{12}$$

The uncertainty expected by the estimation of the film heat transfer coefficient (Δh_f) is calculated according to Eq. (13) based on Eq. (6).

$$\Delta h_f = \sqrt{\left(\frac{\partial h_f}{\partial U}\Delta U\right)^2 + \left(\frac{\partial h_f}{\partial h_{plate}}\Delta h_{plate}\right)^2 + \left(\frac{\partial h_f}{\partial h_{HTF}}\Delta h_{HTF}\right)^2} \tag{13}$$

Where; Δh_{plate} and Δh_{HTF} are the uncertainty of h_{plate} and h_{HTF}, respectively. The accuracies of the utilized individual sensors are listed in Table 3.

3. Analytical analysis

3.1. Thin film evaporation; a theoretical background

During evaporation in a stagnant evaporator like the one investigated in this work, the heat flux densities required for nucleate boiling are not achieved at the prevailing evaporator pressures. Convective boiling is also not to be expected due to the large temperature differences required between the surfaces of the water layer to be evaporated. Furthermore, the filling quantity of the evaporator in such an intermittent adsorption appliance shall be reduced to the minimum required level, in order to minimize the pre-heating and pre-cooling losses. Accordingly, the filling levels of the water required for convective boiling are not available. For the explained reasons, the expected evaporation mechanism is heat conduction through a thin film.

The applied asymmetric plate heat exchanger shall offer the required large heat transfer surface area, in order to realize an effective thin film evaporation. Lang [49] and Westerfeld [50] have introduced and analyzed a set of finned-tube evaporator and adsorber heat exchangers for intermittent adsorption heat pumps. Sato and Niceno [51] have studied nucleate boiling and its transition to film boiling on horizontal surfaces. They reported that, in case the length of the liquid–vapour interface is smaller than the so-called "critical wavelength (λ_C) defined by Eq. (14), the interface becomes stable resulting in a stable film boiling. Otherwise, the interface becomes unstable and nucleate boiling is the dominating evaporation mechanism. The critical wavelength can be considered as the instability limit according to the Rayleigh-Taylor instability as introduced in [52,53].

$$\lambda_C = 2\pi\sqrt{\frac{\sigma}{(\rho_l - \rho_v)\ g}} \tag{14}$$

For the tested water evaporation at 10 to 15 [°C], the critical wavelength amounts to 17.3 [mm]. The applied asymmetric plate heat exchanger is equipped with dimples with a maximum diameter of less than 9 [mm] and a maximum flat surface distance between two successive dimples of less than 12 [mm]. Accordingly, a stable thin film evaporation is expected to take place inside the introduced PHEx.

To achieve a good heat transfer coefficient h_f, with the low thermal conductivity of water (λ_w) of 0.57 [W•m^{-1}•K^{-1}], thin layers of the liquid film are required, which depends on the surface tension of the liquid water (σ) and the surface forces between the phases in contact. Wolf [54] gives the following relationship (Eq. (15)) for the minimum or critical layer thickness, δ_{min} or δ_c, of a liquid film on a flat solid surface:

$$\delta_{min}\ or\ \delta_c = \sqrt{\frac{2\sigma}{\rho g}(1 - cos\theta)} \tag{15}$$

The critical layer thickness is, obviously, a function of the contact angle, which in turn depends on a large number of influencing factors. Upon wetting metallic surfaces with water, contact angles of almost zero degree can generally be achieved [55,56]. In technical applications, however, the contact angle can be higher due to the contamination of the surfaces with wetting-inhibiting substances. Measures to increase wetting, such as the application of a capillary structure on the metal surface by sandblasting or etching, in turn, lead to a sharp reduction in the contact angle [57]. Furthermore, a distinction must be made as to whether the liquid spreads over the surface to be wetted, in which case the contact angle is termed as the advancing contact angle. In case the liquid film contracts over the surface, which is the expected case in our stagnant film evaporator during the adsorption-evaporation process, the contact angle is termed as the receding contact angle [58,59].

A precise statement about the contact angle is difficult due to the complex relationships, since the values contained in the literature for metal-water pairings under vacuum and in the temperature range under study are quite scarce. Hobler [60] gives a value of = 37.7° for the pair aluminum-water, without specifying whether it is an advancing or receding angle. Harmati [57] determined an advance angle of = 39° in spray tests.

To minimize the wetting angle and thus the minimal water layer thickness in the evaporator of adsorption appliances, the evaporator surfaces shall be sandblasted and cleaned in an ultrasonic bath [49]. The experimental observations during the evaporation process of [49] revealed that, with well pretreated, clean evaporator surfaces, minimal layer thicknesses of well below 1 [mm] can be achieved. As the investigated asymmetric plate heat exchanger is a nickel-brazed heat exchanger, the surface of each plate can be simply assumed to be

perfectly clean as the brazing process takes place inside a vacuum oven at around 1100 [°C]. The residuals of the nickel foils can be seen on the surface of the brazed plates with a simple endoscope, which are expected to reduce the contact angle very much (doing the same effect like sandblasting, however in a much cleaner way).

The obtained results of the experimental investigations of the currently studied evaporator shall be applied to derive a relation between the liquid film thickness (δ), the active (wetted) area of the evaporation (A_{wet}) and the film evaporation heat transfer coefficient (h_f). The following paragraphs present the analytical model to account for film evaporation at layer thicknesses greater or equal to the critical film thickness.

3.2. Development of the $h_f - \delta - A_{wet}$ correlations

Upon developing a correlation between the thin-film heat transfer coefficient (h_f), the film thickness (δ) and the wetted evaporator area (A_{wet}), a distinction must be made between three expected evaporation scenarios. In the first scenario (Scenario 1), the thickness of the liquid water film is higher than a critical liquid film thickness (δ_c) (as defined by Eq. (15)), see Fig. 7. Hereby the thickness of the liquid film decreases homogenously with ongoing time (Fig. 7a), whereas the whole plate's area remains fully wetted with liquid (Fig. 7b).

Once the liquid film thickness reaches its critical value δ_c, due to the continuous evaporation of the water, the evaporation mechanism changes, and one of the two following scenarios (Scenarios 2 and 3) shall be encountered. In Scenario 2, see Fig. 8, the liquid film thickness cannot decrease below a critical value and thus remains constant at δ_c over time (Fig. 8a), but the wetted area covered with water starts to shrink continuously as long as the evaporation is still ongoing (Fig. 8b). In other words, the plate's area is partially wetted, and the wetted area is decreasing with time at a constant critical film thickness. In Scenario 3, the value of the critical liquid film thickness δ_c is variable ($\delta_c = f(t)$) due to the existence of the dimples and, consequently, both the wetted area and the film thickness shall change continuously as long as the evaporation is still ongoing.

Based on the above discussion for Scenarios 2 and 3, it can be considered that Scenario 3 is a general case for any non-fully covered thin film evaporation, while Scenario 2 represents a special case of Scenario 3, in which the liquid film thickness does not decrease below the critical or minimum value.

Based on the previous discussion of the three scenarios, the correlated heat transfer coefficient $h_{f,corr}$ can be expressed as:

$$h_{f,corr} = \frac{k_l}{\delta(t)} \frac{A_{wet}(t)}{A_{total}} \tag{16}$$

Where k_l [W•m^{-1}•K^{-1}] is the thermal conductivity of the liquid water, $A_{wet}(t)$ [m^2] is the wetted or the active evaporation area, and $\delta(t)$ [m] is the instantaneous film thickness. Depending on whether the A_{wet} [m^2] is equal to A_{total} [m^2] (Scenario 1) or less (Scenarios 2 and 3), the following equation is developed for the calculation of δ [m].

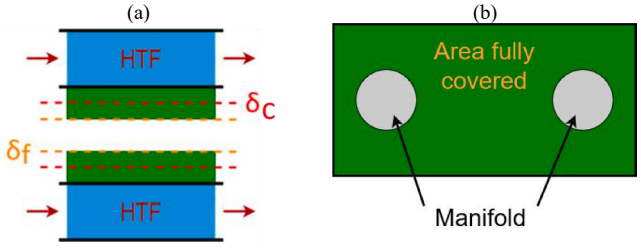

Fig. 7. Scenario 1 of the thin film evaporation. (a) Side view of a volume element, (b) Top view of a plate.

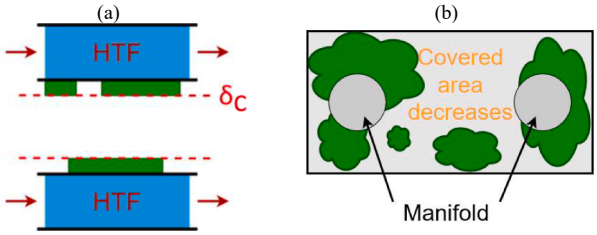

Fig. 8. Scenarios 2 and 3 of the thin film evaporation. (a) Side view of a volume element, (b) Top view of a plate.

$$\delta(t) = \begin{cases} \delta_f(t), A_{wet} = A_{total} (Scenario1) \\ \delta_c = constant, A_{wet} < A_{total} (Scenario2) \\ \delta(t), A_{wet} < A_{total} (Scenario3) \end{cases} \tag{17}$$

$\delta_f(t)$[m] is the liquid film thickness if the film is fully covering the evaporator area, i.e., if the liquid film does cover the whole plates' area. Eq. (18) accounts for $\delta_f(t)$

$$\delta_f(t) = \frac{V_l(t)}{A_{total}} \tag{18}$$

where $V_l(t)$ is the liquid water volume in the evaporator heat exchanger (Eq. (19)). The realization of a liquid film with a thickness of δ_f is not inevitable during an evaporation process as the evaporation process can start with non-fully covered liquid film. In this case, the actual initial thickness of the liquid film will equal δ_c and shall either remain invariant during the whole evaporation time (Scenario 2) or may increase during the evaporation because of the collection of the water in the concave, downward-oriented dimples (Scenario 3). However, the wetted area of the plates in both scenarios (2 and 3) shall shrink with the ongoing time of the evaporation process. The water volume as a function of time can be obtained from the following equation.

$$V_l(t) = V_l(t=0) - \frac{t}{\rho_l . h_{fg}} \int_0^t \dot{Q}_{ev} . dt \tag{19}$$

Hereby h_{fg} [J.kg^{-1}] is the water's latent heat of vaporization and ρ_l [kg.m^{-3}] is the density of liquid water.

The ratio $\frac{A_{wet}}{A_{total}}$ appearing in Eq. (16) is to account for the influence of the active or wetted evaporator area A_{wet} [m^2] on the $h_{f,corr}$, as the $h_{f,corr}$ shall be associated to the A_{total} as done with the evaporation heat transfer coefficient obtained experimentally, i.e. h_f (cf. Eq. (5) & (6)). The active or wetted area during thin film evaporation A_{wet}[m^2] can be determined knowing the current water volume $V_l(t)$ in the evaporator heat exchanger:

$$A_{wet}(t) = \frac{V_l(t)}{\delta(t)} \tag{20}$$

From Eq. (16) and (20) the following equation for the correlated thin-film evaporative heat transfer coefficient can be derived.

$$h_{f,corr}(t) = \frac{k_l}{(\delta(t))^2} . \frac{V_l(t)}{A_{total}} \tag{21}$$

A sensitivity analysis is conducted for every applied set of operating conditions to find the instantaneous film thickness $\delta(t)$ that best fits the $h_{f,corr}$ to the experimentally obtained value of h_f for each time point (t). The best fitted film thickness at a certain time point, $\delta(t)$, is the one that minimizes the sum of the absolute differences between the $h_{f,corr}$ and h_f over a time duration $t - \Delta t$ to $t + \Delta t$. For each couple of the residuals (instantaneous values) of the $h_{f,corr}$ and h_f, the following equation is applied to get the instantaneous δ value, $\delta(t)$.

$$\min_{\delta(t)} \sum_{t-\Delta t}^{t+\Delta t} \left| h_{f,corr}(\delta(t)) - h_f(t) \right| \tag{22}$$

After getting the instantaneous $\delta(t)$ values, Eq. (20) shall be applied to estimate the instantaneous wetted area $A_{wet}(t)$.

3.3. Correlating the evaporator and the adsorber performances

It is well-known, that the prime mover for the evaporation process in an adsorption chiller, heat pump or storage unit is the adsorber performance. Indeed, the size and performance matching between both adsorber and evaporator heat exchanger dictate the temporal behaviour of the encountered combined heat and mass transfer process. If the adsorber HEX is more effective than the evaporator HEX, the pressure is expected to decrease very much, which implies a non-isobaric adsorption process. Indeed, the adsorption potential of the adsorbent and the high heat and mass transfer characteristics of the adsorber HEX results in a high adsorption rate (high time rate of change of the water uptake). If the evaporator is not able to supply the water vapour at the dictated rate, based on the adsorber performance, the pressure shall decrease and, consequently the temperature of the evaporated water is going to decrease compared to the heat transfer fluid temperature. The instantaneous value of the overall evaporator heat transfer coefficient (U) depends, consequently, on the measured evaporator power according to equation (1) and the logarithmic mean temperature difference ($LMTD$) as defined by equations (2) and (3). Under extremely good operation conditions for the adsorber (high evaporator and low adsorption-end temperatures) the expected time rate of change of the water uptake is quite high and, in turn, the pressure reduction. This implies an increase in the $LMTD$ and not necessarily an increase in U. On the contrary, moderate operating conditions would imply moderate pressure reduction and, consequently lower $LMTD$ leading to a higher overall evaporator heat transfer coefficient. In the following paragraphs, we are introducing an attempt to explore the dependency of the evaporator's overall heat transfer coefficient on the adsorption potential and the time rate of change of the water uptake.

As depicted in Eq. (2), the overall heat transfer coefficient in the evaporator (U) is proportional to the evaporator power divided by the logarithmic mean temperature difference ($LMTD$), where the proportional factor is the reciprocal value of the total heat transfer area.

$$U \propto \frac{\dot{Q}_{evap}}{LMTD} \tag{23}$$

As the amount of the evaporated water from the evaporator equals to the amount adsorbed in the adsorber, the evaporator power $\dot{Q}_{evap}$ [W] can be also expressed by the following equation.

$$\dot{Q}_{evap} = m_{ads} . \frac{dw(t)}{dt} . h_{fg} \tag{24}$$

Herein, m_{ads} [kg] is the dry mass of the adsorbent filled inside the adsorber heat exchanger, $\frac{dw(t)}{dt}$ [s^{-1}] is the time rate of change of the instantaneous water uptake, which is dictated by the adsorber HEX, h_{fg} [$J.kg^{-1}$] is the latent heat of evaporation corresponding to the prevailing evaporator temperature T_{evap}. From the above equation, the following relationship can be formulated.

$$\dot{Q}_{evap} \propto \frac{dw(t)}{dt} \tag{25}$$

As depicted in Eq. (3), the LMTD is a function in $T_{HTF,in}$, $T_{HTF,out}$ and T_{ref}. The instantaneous change in the LMTD value is mainly due to the change in the T_{ref}. Recalling that $T_{HTF,in}$ is constant during each conducted adsorption-evaporation process. Due to the suction of water vapour by the adsorber, the evaporation process in the evaporator is induced leading to a temporal drop in the T_{ref} value and, consequently, a drop in the $T_{HTF,out}$. It can, therefore, be considered that the LMTD is mainly a function in T_{ref}.

$$LMTD = f(T_{HTF,in}, T_{HTF,out}, T_{ref}) = f(T_{ref}) \tag{26}$$

T_{ref} is measured implicitly during the conducted adsorption-evaporation processes by means of measuring the temporal vapour pressure in the evaporator (P_{evap}). Tetens equation is used to estimate the temporal T_{ref} out of the measured pressure inside the evaporator [61] as presented in Eq. (27).

$$T_{ref}(t) = T_{sat}\left(P_{evap}(t)\right) = -237.3\left(\frac{ln(P_{evap}(t)/6.1078)}{ln(P_{evap}(t)/6.1078) - 17.27}\right) \tag{27}$$

In Eq. (27), P_{evap} is in [mbar] and the obtained T_{ref} is in [°C]. From Eq. (26) and (27)

$$LMTD = f(P_{evap}) \tag{28}$$

The Linear Driving Force (LDF) model [62,63] gives a relationship for $\frac{dw}{dt}$ as a function in the instantaneous water uptake ($w(t)$) the evaporator pressure P_{evap}, the instantaneous vapor pressure inside the adsorbent (P_{ad}) and the instantaneous adsorbent temperature T_{ad}. The following relationship for P_{evap} can, therefore, be considered.

$$P_{evap} = f\left(P_{ad}, T_{ad}, \frac{dw}{dt}\right) \tag{29}$$

At the same time, the adsorption potential or the so-called "Dubinin-Polanyi" potential (A) [$J.kg^{-1}$] [64] also represents a relation between P_{ad} and T_{ad} as follows.

$$A = -R.T_{ad}.\ ln\left(\frac{P_{ad}}{P_{sat}}\right) = f(P_{ad}, T_{ad}) \tag{30}$$

Hereby R [$kJ.mol^{-1}.K^{-1}$] is the universal gas constant and P_{sat} [Pa] is the saturated vapour pressure corresponding to the instantaneous adsorbent temperature T_{ad}. Eliminating T_{ad} and P_{ad} from the relationships (29) and (30), the following functional relationship can be formulated to couple the $LMTD$ (Eq. (28)) and both the adsorption potential and the time rate of change of the water uptake.

$$LMTD = f\left(A, \frac{dw}{dt}\right) \tag{31}$$

From the relationships (23), (25) and (31), the following dependency is expected for the overall evaporator heat transfer coefficient on the adsorption potential and the time rate of change of the water uptake inside the adsorbent.

$$U \propto \frac{\frac{dw}{dt}}{f\left(A, \frac{dw}{dt}\right)} \approx f\left(A, \frac{dw}{dt}\right) \tag{32}$$

As T_{ad} cannot be directly measured, the instantaneous values of the adsorption potential (A) [$kJ.kg^{-1}$] are estimated out of the equilibrium function for the water uptake, w of the utilized adsorbent (Siogel) inside the adsorber heat exchanger [44].

$$A = E \times \left(-ln\left(\frac{w}{w_o}\right)\right)^{\frac{1}{n}} \tag{33}$$

Where $w_o = 0.38$ [$kg.kg^{-1}$], $E = 220$ [$kJ.kg^{-1}$] and n = 1.1.

In the result section, the type of the function, which best describe the developed functional relationship (32) will be presented and the obtained results will be discussed.

4. Results

4.1. Visualized investigation on the evaporation mechanism

The visualization of the water evaporation on the surface of one of the refrigerant channels and one of the two refrigerant vapour manifolds inside the investigated evaporator plate heat exchanger is utilized to

determine the evaporation mechanism prevailing during the conducted adsorption-evaporation processes. A number of screenshots taken from the video film recorded by endoscope (1) during the adsorption-evaporation process under the operating condition of 15/30/90[°C] are presented in Fig. 9, showing the vision of endoscope (1) between two successive HTF channels. Six inclined surfaces of different dimples and the flat horizontal surfaces connecting them can be distinguished [35]. The dimples appearing in the vision of endoscope (1) are categorized into (i) two opposite, deep and concave dimples, (ii) two opposite, shallow and concave dimples, and (iii) two opposite and convex dimples brazed together at their interfacial surface. As the thin liquid film is transparent, the visualization of the free surface of the liquid film in the refrigerant channel cannot be clearly observed by the illustrated screenshots. Therefore, red, and blue contours on the boundary of the liquid film covering the surface of the deep and shallow dimples, respectively, have been added to all screenshots illustrated in Fig. 9. In addition, a short video (Video 1) from the recording of endoscope (1) is attached. The video shows the movement (shrinking) of the liquid film during the evaporation, which is detectable by the change in the brightness of the liquid film.

It can be noticed that, at the beginning of the evaporation process (Fig. 9a) the dimples were covered with a liquid film. After about 5 min of evaporation, a small amount of liquid was evaporated, and the liquid film start to shrink. With ongoing time, the liquid film especially in the upper deep concave dimple shrinks noticeably and disappeared completely (Fig. 9b). Lastly, the liquid film in the lower deep concave dimple evaporated completely and the area appearing in the vision of endoscope (1) became dry at the end of the evaporation process (Fig. 9c). Indeed, the test unit is filled with 225 [g] of degassed water, which is higher than the total water amount that can be exchanged between the adsorber and evaporator under the most severe applied operating condition ($T_{evap} = 15$ [°C] and $T_{ads-end}$=$T_{cond} = 30$ [°C]). This means that the visualization of a totally dry area in a refrigerant channel as depicted by the viewed segment of endoscope (1) and (Fig. 9d), does not imply that the whole evaporator shall be empty at the end of the evaporation process. Based on the above discussion and, most specifically, the observed film shrinking in all investigated videos from the beginning till the end of the conducted adsorption-evaporation processes, it can be concluded that partially covered (discontinuous) thin film evaporation is the evaporation mechanism taking place in the investigated asymmetric plate heat exchanger acting as a horizontally placed, stagnant evaporator for the adsorption chilling unit presented in Fig. 1.

Fig. 10 depicts two screenshots taken from a video film of endoscope (2), which has been recorded simultaneously with the video film of endoscope (1). A short video (Video 2) from the recording of endoscope (2) is attached as well. The visualization of endoscope (2) presented in Fig. 10a illustrates that from the start of the adsorption-evaporation process the bottom of the manifold is almost dry. However, during the first few seconds after the start of the adsorption-evaporation process, the free water surface at the entrance into all parallel evaporation domains are very much disturbed (Fig. 10a). This is attributed to the high adsorption rate at the beginning of the adsorption-evaporation process. With ongoing time, the amount of the liquid water existing at the inlet of the refrigerant channels is reduced very much and quite thin liquid film on the edges of the refrigerant channels' inlet was realized. Finally, this thin liquid film on the edges of the refrigerant channels' moves (shrinks) into the inside of the successive evaporation domains (see Fig. 10b and Video 2). Similar results were obtained in the tests at the other boundary conditions.

4.2. Evaporator power and its overall heat transfer coefficient

The measured temporal evaporator powers of all conducted adsorption-evaporation processes are depicted in Fig. 11. The uncertainty analysis of the obtained $\dot{Q}_{evap}$-values ($\Delta\dot{Q}_{evap}$) according to Eq. (11) in section 2.4 results in a maximum relative error of ± 2 %. The evaporator power obtained from the adsorption-evaporation process conducted at 15/30/90[°C] is nearly twice as high as that conducted at 10/35/90[°C], whereas the evaporator power obtained at 15/35/90 [°C] is almost equal that obtained at 10/30/90[°C]. This implies that the time rate of change of the water uptake at the condition 15/30/90 is almost twice as high as that at 10/35/90 °C operating condition. The cooling effect, which is the time integral of the evaporator power as described by Eq. (24) is directly proportional to the differential water uptake Δw [kg.kg^{-1}] of the adsorber. Strictly speaking, Δw equals 0.182 [kg.kg^{-1}] at 15/30/90[°C], and 0.094 [kg.kg^{-1}] at 10/35/90[°C] [44]. At the operating conditions 15/35/90[°C] and 10/30/90[°C], almost the same differential water uptakes (Δw) have been obtained; namely, 0.129 [kg.kg^{-1}] and 0.123 [kg.kg^{-1}], respectively. The measured evaporator power curves at both boundary conditions (green and blue curves in Fig. 11) are almost identical, which implies similar temporal course of variation of their respective $\frac{dw}{dt}$.

Fig. 12 presents the test results to investigate the repeatability of the obtained results out of our experimental setup. Indeed, almost identical evaporator power curves have been measured upon repeating the adsorption-evaporation process at 15/30/90 [°C] (Fig. 12(a)) and at 10/35/90 [°C] (Fig. 12(b)). The maximum deviation between the measured curves is less than ± 0.3 %, which proves the repeatability of the experimental setup and the measuring devices.

Fig. 13 shows the estimated evaporator's overall heat transfer coefficient according to Eq. (2) for repeated adsorption-evaporation processes, at 15/30/90 [°C] (Fig. 13(a)) and at 10/35/90 [°C] (Fig. 13(b)). Here also quite similar U curves have been obtained for every applied set of operating condition. This indicates a high stability of the established experimental setup. Since the experimental data of $\dot{Q}_{evap}$ and the *LMTD* obtained at the beginning of the adsorption-evaporation processes are

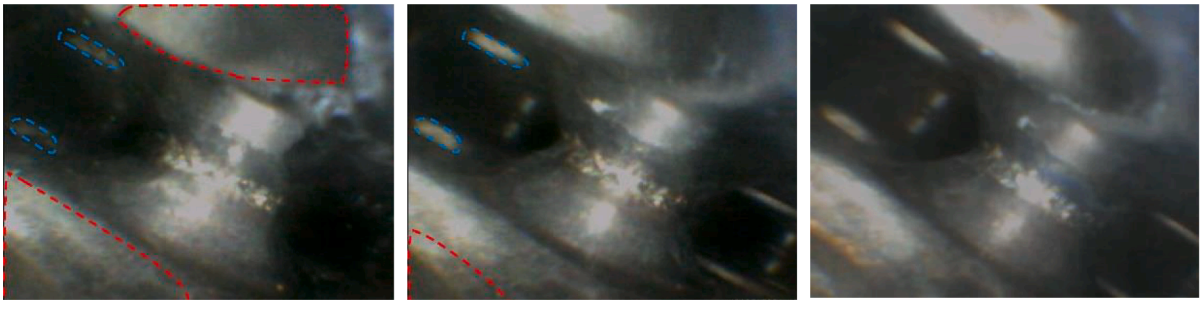

(a) (b) (c)

Fig. 9. Screenshots from endoscope (1) between the plates. (a) at the start of the evaporation, (b) upper deep and concave dimple becomes almost dry, (c) at the end of the evaporation.

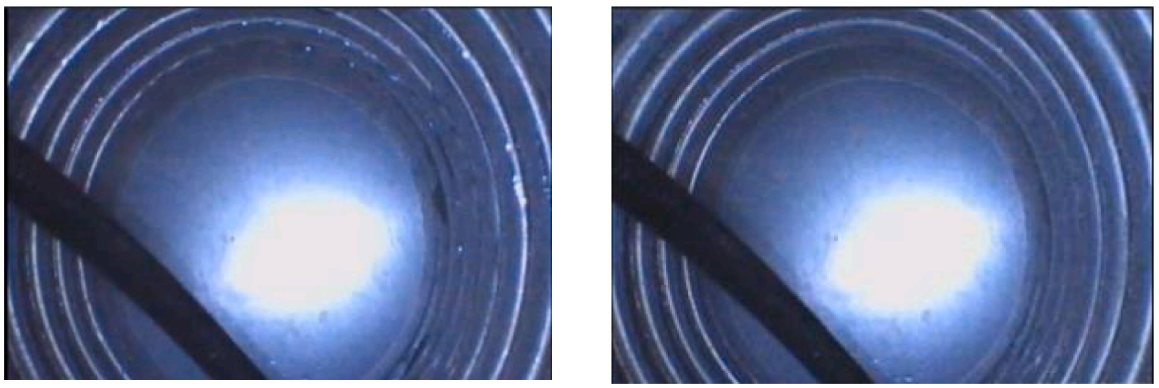

(a) (b)

Fig. 10. Screenshots from endoscope (2) in the manifold. (a) at the start of the evaporation, (b) at the end of the evaporation.

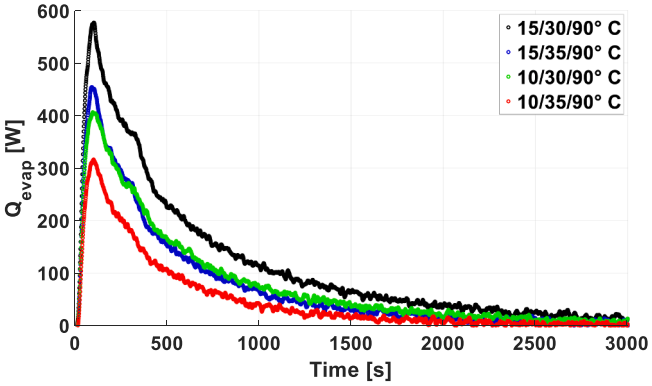

Fig. 11. Calculated evaporator power for all applied operating conditions.

close to zero, the calculated U-values are characterized by fluctuations with a higher level of uncertainty. The same is valid after 2400 s from the beginning of each process, where the equilibrium condition is approached and, consequently, the temperature difference becomes so low that the uncertainty in measuring that temperature difference and, accordingly, the U-value does remarkably increase. Therefore, we fixed the analysis of the experimental results to the period between 60 s and 2400 s. In the fixed time range for the analysis, it was found that the uncertainty of $\dot{Q}_{evap}$ and the $LMTD$, i.e. $\Delta\dot{Q}_{evap}$ and $\Delta LMTD$ are less than $\pm$ 2 % and $\pm$ 14 %, respectively. The corresponding uncertainty of U (ΔU) is estimated to be less than $\pm$ 20 %.

4.3. Individual contributions to the overall heat transfer coefficient

Applying the Eqs (1) to (9), the contribution of each individual heat transfer coefficient to the overall heat transfer coefficient under the operating condition 15/30/90 [°C] are estimated and presented in Fig. 14. It is a basic heat transfer knowledge that the overall heat transfer coefficient (U) shall be less than the least heat transfer coefficient in the serial connection according to Fig. 6, for which the total heat transfer resistance is expressed by Eq. (4).

It is clearly visible that the evaporation heat transfer coefficient on the refrigerant side h_f is the one with the major influence on U, followed by the heat transfer coefficient on the HTF side (h_{HTF}) and the heat transfer coefficient due to conduction through the plate's wall h_{plate}. Based on Eq. (6), the observed temporal fluctuation appearing in h_f are mainly caused by those existing in U, which are attributed to the main uncertainty in estimating the LMTD as described before. The uncertainty in h_f (Δh_f) based on Eq. (13) is estimated to be less than $\pm$ 20 % in the determined time range for the analysis.

4.4. Fitting $h_{f,corr}$ to $h_{f,exp}$

Fig. 15 illustrates the temporal development of; (i) the experimentally obtained overall heat transfer coefficient U of the evaporator (in black), (ii) the experimentally obtained thin film evaporation heat transfer coefficient $h_{f,exp}$ (in red out of Eq. (6)) and (iii) the analytically obtained thin film evaporation heat transfer coefficient $h_{f,corr}$ (in blue according to Equations (16–21)) that best fit the experimentally obtained results at all applied sets of operating conditions. As shown in Fig. 15a-d, the value of h_f over the whole investigation boundary conditions decreases from an initial value in the range of 1330 $\pm$260 down

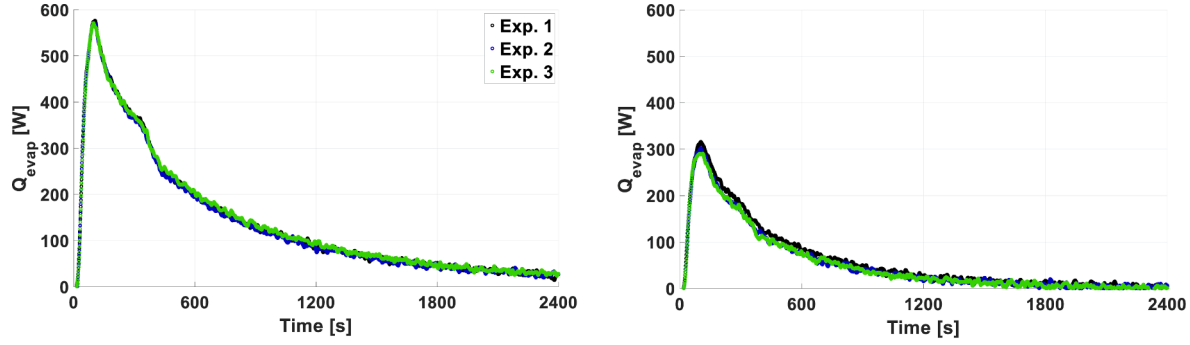

(a) (b)

Fig. 12. Calculated evaporator power for repeated adsorption evaporation processes at two different operating conditions. (a) 15/30/90[°C], (b) 10/35/90[°C].

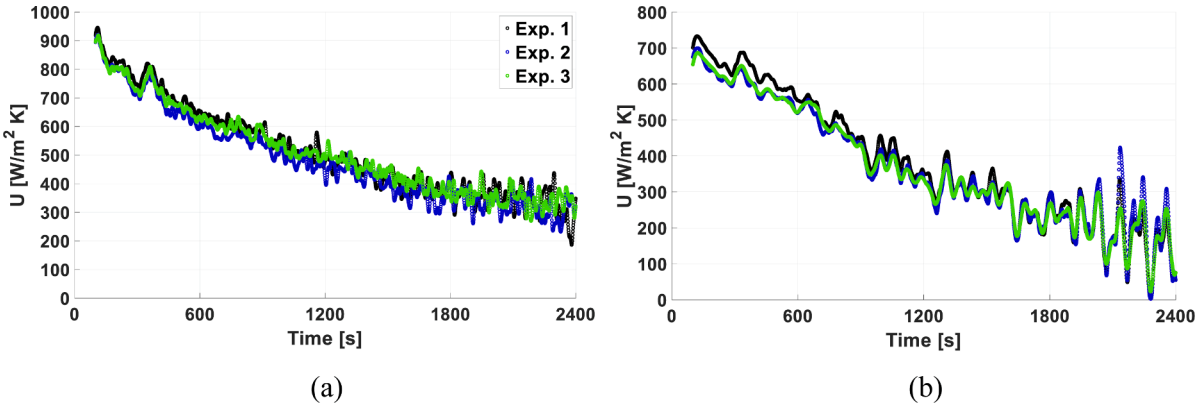

Fig. 13. Calculated overall heat transfer coefficient (U) of the evaporator for repeated adsorption evaporation processes at two different operating conditions. (a) 15/30/90 [°C], (b) 10/35/90 [°C].

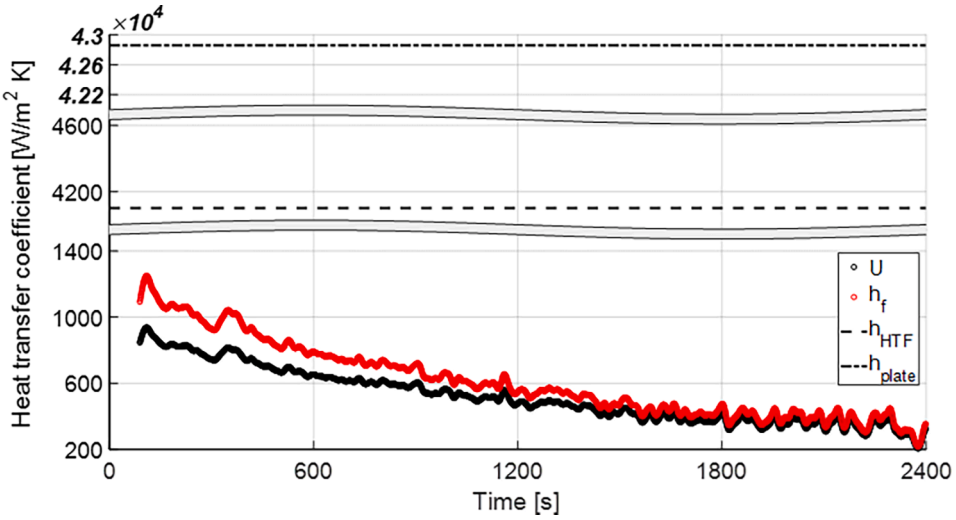

Fig. 14. Contributions to the overall heat transfer coefficient.

to 160 ± 32 [W•m^{-2}•K^{-1}] upon approaching the equilibrium condition at the end of each process. As illustrated in Fig. 15a-d, both U and h_f values do decrease from a higher value, at the beginning of each process, with time. This implies that each investigated process does start with a partially covered thin film ($A_{wet} < A_{total}$), which excludes Scenario 1 from the further analysis (cf. Eq. (17)). The obtained values of h_f are very close to the range of the evaporation heat transfer coefficient found for a finned tube flooded evaporator [29], which varies between 465 and 1390 [W•m^{-2}•K^{-1}] in the evaporator temperature range between 5 and 20 [°C]. In addition, the evaporation heat transfer coefficient measured for a capillary-assisted evaporator with fine fins on the tube's outer surface [65], has been found in range between 500 and 1000 [W•m^{-2}•K^{-1}], which is not far from the measured range of h_f inside the plate heat exchanger presented in this work. In [30,31], capillary assisted evaporator tubes have been investigated against a vacuum pump and a condenser, respectively, showing a very promising performance. Strictly speaking, evaporator U-values up to 5 [kW•m^{-2}•K^{-1}] have been measured resulting in thin-film evaporative heat transfer coefficients of up to 11,300 [W•m^{-2}•K^{-1}]. Because of the applied constant rate of evaporation, dictated by the vacuum pump [30] and the condenser at a lower temperature [31], both overall evaporator and thin film evaporation heat transfer coefficients do increase with time, in contrast to the behaviour obtained in this work, in which the evaporator works against a real adsorber heat exchanger. The presented temporal courses of U and h_f in Figs. 14 and 15 decrease with time because the driving force of evaporation; namely, the adsorption rate decreases with time approaching the equilibrium state at each operating condition. Indeed, the evaporator performance is highly dependent on the adsorber performance, as already explained in section 3.3 and will be presented in section 4.6. The extremely good values presented in [30,31] stay, therefore, as upper limits, until the proposed evaporator heat exchangers will be applied and measured against an adsorber heat exchanger.

4.5. Correlating the obtained evaporative heat transfer coefficient h_f to δ and A_{wet}

Fig. 16 depicts the temporal development of the film thickness δ (in black) and the active or wetted to total area ratio A_{wet}/A_{total} (in red) of the thin liquid film covering the plates' surface in the evaporator at all applied sets of operating conditions. As illustrated in Fig. 16a, the variation of the liquid film thickness δ is very limited at the operating condition of 15/30/90[°C]. The film starts with a thickness of $\delta = 0.35$ [mm], which remains constant within ±0.01 [mm] over the whole adsorption evaporation time. This implies a constant film thickness, while the wetted to total area ratio decreases continuously with time. This case matches exactly Scenario 2 as described in detail in section 3.2. The quite low film thickness of 0.35 [mm] can be attributed to the very clean surface due to vacuum brazing and the sandblasting like effect by the residuals of the nickel folie, which are observable on the evaporator

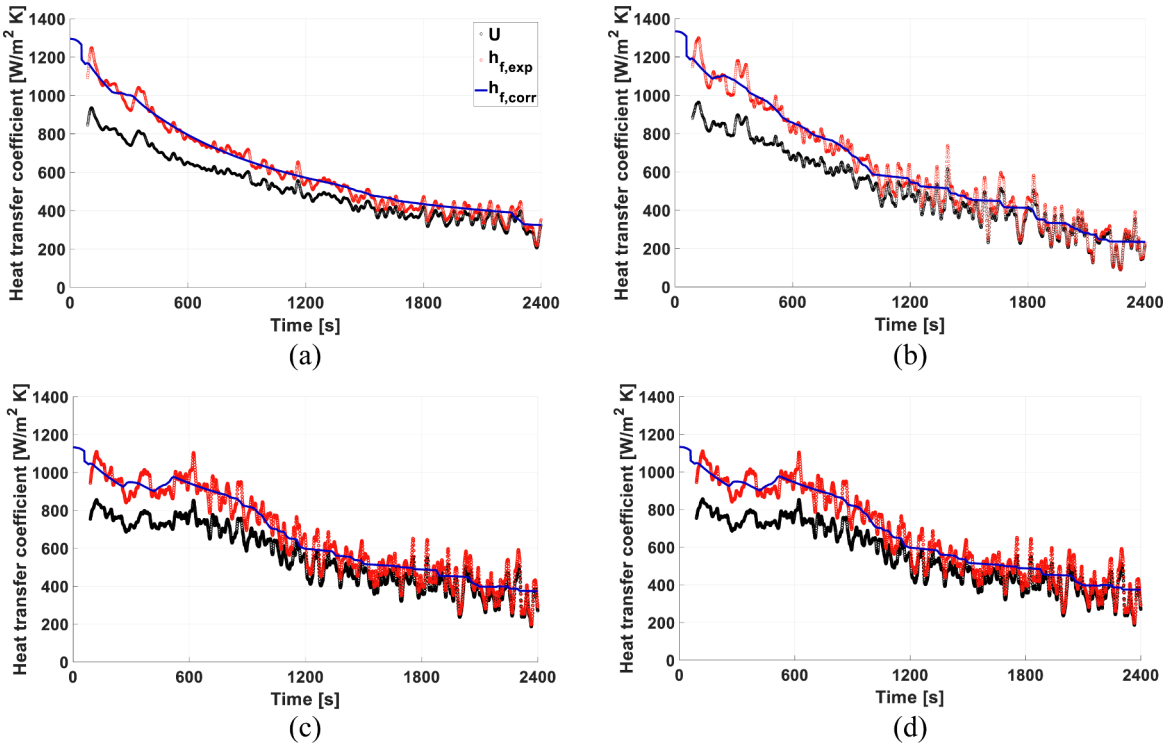

Fig. 15. Experimentally obtained U and $h_f(h_{f,exp})$ together with the correlated thin film heat transfer coefficient ($h_{f,corr}$) at all applied sets of operating conditions, (a) 15/30/90 [°C], (b) 15/35/90 [°C], (c) 10/30/90 [°C] and (d) 10/35/90 [°C].

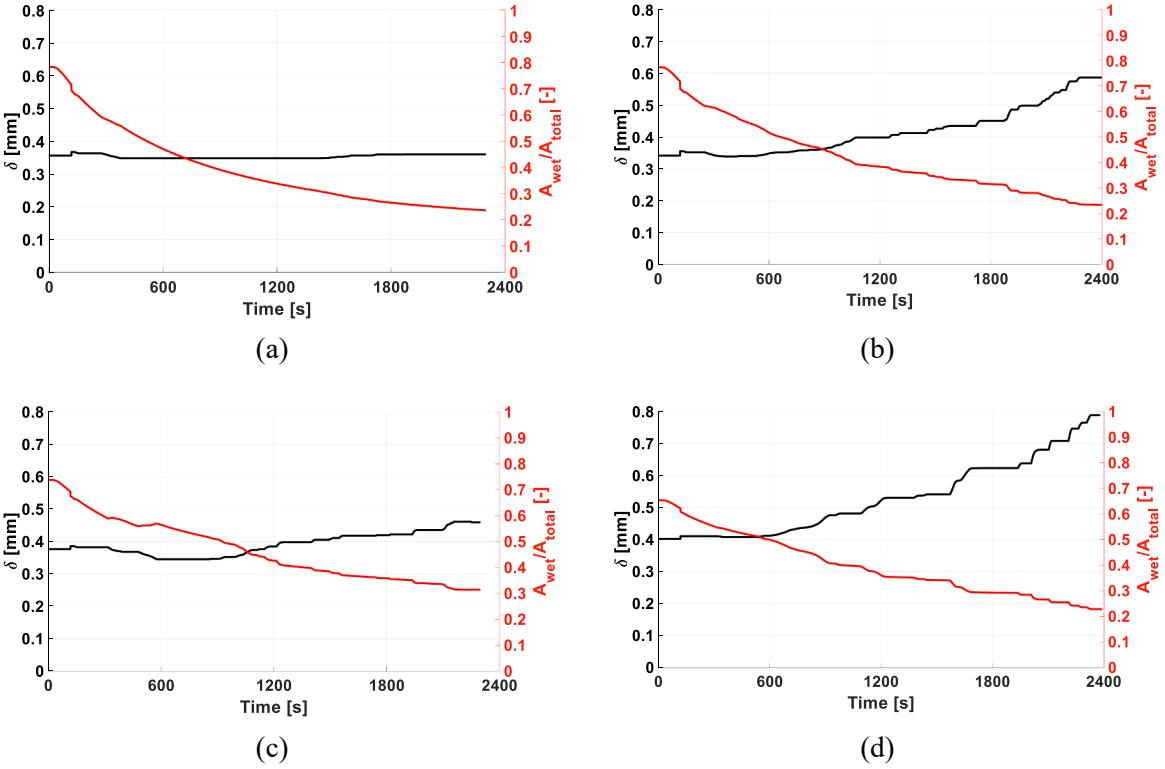

Fig. 16. Temporal development of the thin film thickness (δ) and the wetted area to total area ratio (A_{wet}/A_{total}), at all applied sets of operating conditions, (a) 15/30/90 [°C], (b) 15/35/90 [°C], (c) 10/30/90 [°C] and (d) 10/35/90 [°C].

surface.

The temporal developments of δ (in black) and A_{wet} (in red) obtained at all other applied sets of operating conditions, depicted in Fig. 16b-d, are in accordance with Scenario 3, in which both the δ and A_{wet} do vary with time. It can be even observed that, during the first 10 min of each process, the film thickness remains constant while A_{wet}/A_{total} decreases,

which implies that Scenario 2 is valid over that period. After that time Scenario 3 is realized and continues till the end of the evaporation process. It is worth to notice that the value of δ tends to increase for the three above mentioned sets of operating conditions, as depicted in the Fig. 16b-d. As mentioned in section 3.2, in case of realizing partially covered, thin film evaporation on a flat surface, a constant and uniform film thickness equal to a minimum or critical value (δ_{min} or δ_c) shall be encountered (Scenario 2). However, the existence of the different dimples on each plate of the studied plate heat exchanger can lead to spatial and temporal variation in the thickness of the partially covered film. In other words, realizing constant film thickness in only a special case, at 15/30/90 [°C], while increasing film thickness in the other cases can be interpreted by the effect of the dimples. It is important to emphasize that the temporal film thickness discussed through this work ($\delta(t)$) refers to the instantaneous average thickness of the liquid film, which partially covers the plates' surface of the evaporator. This means that a spatial distribution of the film thickness is expected. Due to the gravity effect, it is expected that on the lower plate of a refrigerant channel, the thickness of the liquid film covering the bottom of the concave, deep and shallow, dimples is higher than the thickness of the film covering the flat surfaces between the dimples of this plate. In fact, the liquid film thickness should be thinner on the flat surfaces between the dimples and increase gradually along the inclined surfaces of the concave dimples towards their centerlines, as observed upon investigating a thin film of water evaporation on spherical, concave and downward oriented surfaces [66]. Concerning the upper plate, the film thickness distribution shall be the opposite case compared to the one described for the lower plate. This means that the liquid film thickness should be thinner on the top plates' concave dimples and increase gradually along the inclined surfaces towards the flat surfaces between the dimples.

The evaporation and, consequently, the shrinking of the thin liquid film leads to tearing the film in several segments. The collection, even partially, of the separated film segments in the lower concave dimples, due to the gravity effect, leads to a continuous increase in film thickness in the lower dimples. This explains the slight increase in the average film thickness observed in Fig. 16.b-d after the first 10 to 15 min. The high rate of adsorption, which dictates a high evaporation rate may change the situation and results in an invariant film thickness. The above interpretation probably explains why the high evaporation rate associated with the operating condition 15/30/90 [°C] has resulted in an almost invariant average film thickness as depicted in Fig. 16.a at the operating condition 15/30/90 [°C].

Indeed, the existence of a complex topology (such as dimples) on the plates' surface does increase the heat transfer area of the evaporator and enhance the convective heat transfer on the HTF side. However, the above discussion shows the necessity for more dedicated investigations and for a careful design of the plates' topology. Based on Eq. (15) and the presented results of the film thickness in Fig. 16, the contact angle (θ) lies between 11° and 16° for water on the tested heat exchanger (Nickel-brazed stainless steel) under the listed operating conditions in Table 4. As the liquid film contracts with time over the evaporator's surface, the estimated contact angles are receding contact angles as defined in [58,59]. The quite low contact angles are attributed to the very clean evaporation surface because of the applied vacuum brazing process.

4.6. Adsorber-Evaporator performance correlation

Based on the discussion in section 3.3 and, most specifically Eq. (32), the "curve fitting" facility built in MATLAB® has been used to find the most suitable functional relationship between the evaporator's overall heat transfer coefficient (U) and the adsorption potential (A) and the time rate of change of the water uptake ($\frac{dw}{dt}$) of the adsorber. The following relation has been found,

$$U\alpha\left(\frac{dw/dt}{A}\right)^{n} \tag{34}$$

With n equal to 0.5, a linear relation between U and $\sqrt{\frac{dw/dt}{A}}$ is observed. Table 5 gives the slopes obtained for the four applied sets of operating conditions. The coefficient of determination (R^2) values are also presented in Table 5.

Fig. 17 presents the experimentally measures Uvalues (scattered red circles) as a function of the term $\sqrt{\frac{dw/dt}{A}}$ at the four applied sets of operating conditions. The solid black lines represent the linear fitting with the given slopes in Table 5. The dashed black lines represent the linear fitting with the average slope of 1.089E + 06. It can be concluded that, a linear relationship does exist between U and $\sqrt{\frac{dw/dt}{A}}$ for the introduced test unit in Fig. 1 under each set of the investigated operating conditions.

In order, however, to check, whether the linear relationship between U and $\sqrt{\frac{dw/dt}{A}}$is valid without limitations or may have an upper limit, both temporal values are presented in Fig. 18. As can be seen in Fig. 18. a, the term variation of $\sqrt{\frac{dw/dt}{A}}$ attains its maximum value at the operating condition 15/30/90 [°C] followed by the two operating conditions 15/35/90 and 10/30/90 [°C]. The least values of the term variation of $\sqrt{\frac{dw/dt}{A}}$ are obtained at the operating condition 10/35/90 [°C]. Unless at the first operating condition 15/30/90 [°C] the temporal U values, depicted in Fig. 18.b, do follow the same trend with time as the U values do. Indeed, the maximum obtained evaporator power takes place at the operating condition 15/30/90 [°C], as depicted in Fig. 11, which is associated with the highest $\sqrt{\frac{dw/dt}{A}}$ values (cf. Fig. 18.a). Both results do not, necessarily, mean that the evaporator's overall heat transfer coefficient $\sqrt{\frac{dw/dt}{A}}$ shall attain its maximum value as depicted in Fig. 18.b. Indeed, the high adsorption rate $\sqrt{\frac{dw/dt}{A}}$ results in a severe reduction in the vapour pressure, and consequently, in the refrigerant (water) temperature (T_{ref}) leading to an increase in the LMTD. Based on Eq. (2), the higher LMTD is responsible for the lower U-values despite the measured higher evaporator power. It can, therefore, be concluded that a linear relationship does exist between $\sqrt{\frac{dw/dt}{A}}$ and the evaporator's overall heat transfer coefficient U until a certain threshold for the $\sqrt{\frac{dw/dt}{A}}$ values, which is defined by the green curve in Fig. 18.a representing the operating condition of 10/30/90 °C. Beyond that threshold, the U values tend to decrease again because the LMTD increases due to the induced reduction in the vapour pressure inside the evaporator by the excessively high adsorption rate ($\sqrt{\frac{dw/dt}{A}}$).

5. Conclusion

This communication presents the first experimental study on the application of an asymmetric plate heat exchanger, with a closed structure and a horizontal orientation, to act as a stagnant water evaporator heat exchanger under typical operating conditions of an adsorption heat transformation appliance.. The main outcomes of this study can be summarized as follows:

Table 5

Slope and R^2 values of the linear fittings,U vs..$\sqrt{\frac{dw/dt}{A}}$

Operating conditions [°C]	Slope[J.m^{-1}.kg$^{-0.5}$.K$^{-0.5}$]	R^2
15/30/90	1.023E + 06	0.9794
15/35/90	1.168E + 06	0.9545
10/30/90	1.045E + 06	0.9101
10/35/90	1.123E + 06	0.9469

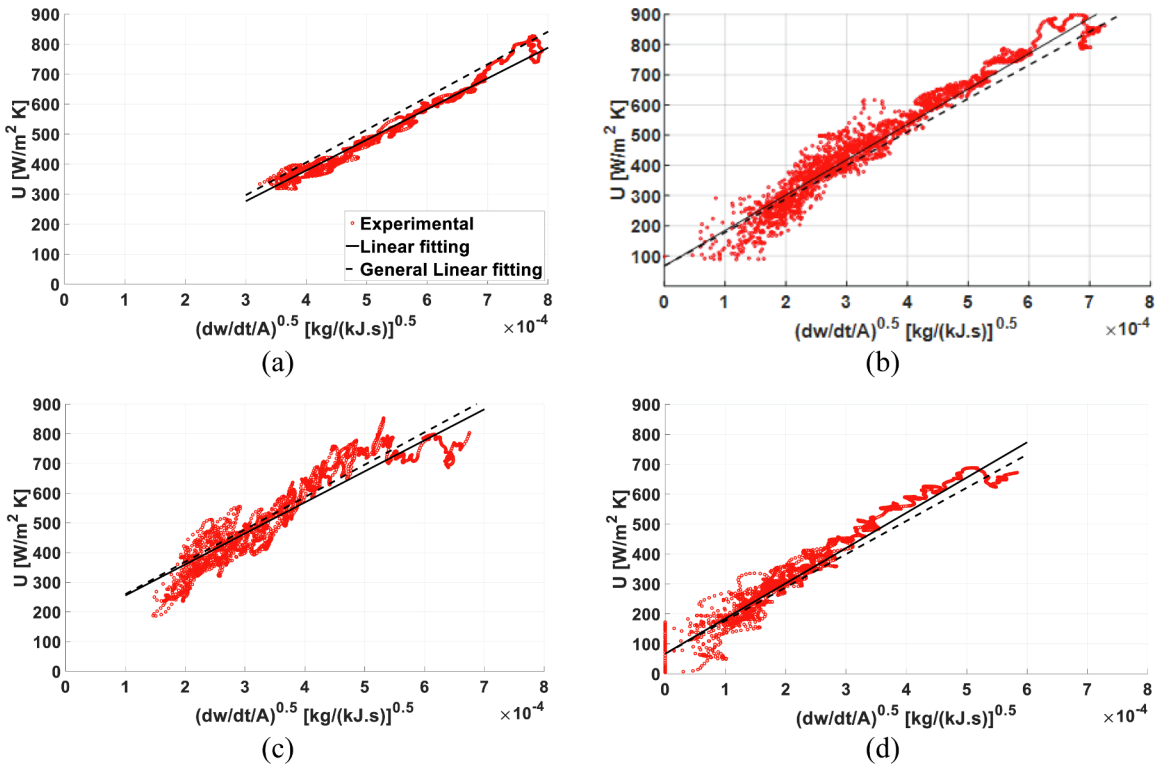

Fig. 17. Variation of *U*against the term $\sqrt{\frac{dw/dt}{A}}$ for all applied sets of operating conditions. (a) 15/30/90 [°C], (b) 15/35/90 [°C], (c) 10/30/90 [°C] and (d)10/35/90 [°C]. Red scattered points represent experimental data, solid and dashed black lines represent the linear fittings. (For interpretation of the references to colour in this figure legend, the reader is referred to the web version of this article.)

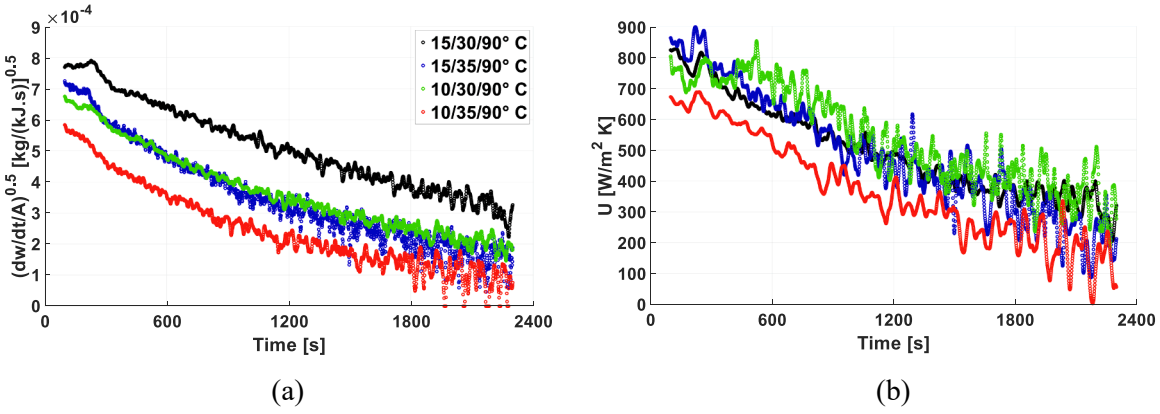

Fig. 18. Temporal variation of the term $\sqrt{\frac{dw/dt}{A}}$ and U at all applied sets of operating conditions, (a) variation of $\sqrt{\frac{dw/dt}{A}}$, (b) variation of U

- Partially covered (discontinuous) thin film evaporation mechanism was identified by the inserted endoscopes.
- The thermal resistance related to the evaporation heat transfer coefficient (h_f) dominates the total heat transfer resistance and, consequently, the evaporator's overall heat transfer coefficient (U) of the investigated evaporator.
- The evaporation heat transfer coefficient (h_f) of the investigated evaporator varies from 1330 ±260 [W•m^{-2}•K^{-1}] at the beginning of the adsorption-evaporation processes to a minimum of 160 ± 32 [W•m^{-2}•K^{-1}] upon reaching the end of each process.
- During the evaporation in the investigated plate heat exchanger two scenarios of the following three different scenarios took place, namely Scenario 2 and 3,
- ***Scenario 1***: δ decreases, while $A_{wet} = A_{total}$ and remains invariant
- ***Scenario 2:***δ equals critical value ($\delta = \delta_c$) and remains invariant, while $A_{wet} < A_{total}$ and decreases continuously.
- ***Scenario 3***: both δ and A_{wet}/A_{total} vary with time.
- The values of δ and A_{wet}/A_{total} that best fit the experimental data are in the range of 0.34 to 0.78 [mm] and 0.16 to 0.78, respectively.
- The overall heat transfer coefficient of the evaporator U is linearly proportional to the adsorption rate defined as $\sqrt{\frac{dw/dt}{A}}$, however until a certain threshold, beyond which U decreases because of the excessive pressure reduction and, consequently the increase in the logarithmic mean temperature difference.

The results obtained in this study imply the appropriateness of application, which could bring several advantages in terms of the system compactness and, accordingly, the specific power density of the system.

Besides, the construction cost of the adsorption appliance may be considerably reduced if the closed-structure PHEs are adopted for use, as there is no need to place the evaporator/condenser inside a vacuum tight chamber, which is quite bulky and costly. The extremely durable operation because of the no corrosion potential is a special added advantage of the introduced technology (Nickel brazing of Stainless-Steel sheets). More investigations are needed, however, to define and optimize the design rules of such special plate heat exchangers for the application in adsorption heat transformation appliances.

Funding

This project has received funding from the European Union's Horizon 2020 research and innovation program under grant agreement No 764025 (SWS-HEATING).

CRediT authorship contribution statement

Makram Mikhaeil: Conceptualization, Methodology, Investigation, Formal analysis, Writing – original draft. **Sebastian Nowak:** Methodology, Investigation, Writing – original draft. **Valeria Palomba:** Methodology, Writing – review & editing. **Andrea Frazzica:** Funding acquisition, Writing – review & editing. **Matthias Gaderer:** Supervision, Writing – review & editing. **Belal Dawoud:** Funding acquisition, Project administration, Supervision, Conceptualization, Methodology, Formal analysis, Writing – review & editing.

Declaration of Competing Interest

The authors declare that they have no known competing financial interests or personal relationships that could have appeared to influence the work reported in this paper.

Data availability

Data will be made available on request.

Acknowledgements

The authors would like to thank the BayWISS Joint Academic Partnership "Energy" for their appreciated support.

Appendix A. Supplementary material

Supplementary data to this article can be found online at https://doi.org/10.1016/j.applthermaleng.2023.120525.

References

[1] L. Wang, R. Wang, J. Wu, Y. Xu, S. Wang, Design, simulation and performance of a waste heat driven adsorption ice maker for fishing boat, Energy 31 (2006) 244–259, https://doi.org/10.1016/j.energy.2005.03.006.
[2] T. Miyazaki, A. Akisawa, The influence of heat exchanger parameters on the optimum cycle time of adsorption chillers, Appl. Therm. Eng. 29 (2009) 2708–2717, https://doi.org/10.1016/j.applthermaleng.2009.01.005.
[3] A. Allouhi, T. Kousksou, A. Jamil, T. el Rhafiki, Y. Mourad, Y. Zeraouli, Optimal working pairs for solar adsorption cooling applications, Energy 79 (2015) 235–247, https://doi.org/10.1016/j.energy.2014.11.010.
[4] D.B. Boman, D.C. Hoysall, D.G. Pahinkar, M.J. Ponkala, S. Garimella, Screening of working pairs for adsorption heat pumps based on thermodynamic and transport characteristics, Appl. Therm. Eng. 123 (2017) 422–434, https://doi.org/10.1016/j.applthermaleng.2017.04.153.
[5] Q. Cui, G. Tao, H. Chen, X. Guo, H. Yao, Environmentally benign working pairs for adsorption refrigeration, Energy 30 (2005) 261–271, https://doi.org/10.1016/j.energy.2004.05.005.
[6] A. Frazzica, A. Freni, Adsorbent working pairs for solar thermal energy storage in buildings, Renew. Energy 110 (2017) 87–94, https://doi.org/10.1016/j.renene.2016.09.047.
[7] A.N. Shmroukh, A.H.H. Ali, S. Ookawara, Adsorption working pairs for adsorption cooling chillers: a review based on adsorption capacity and environmental impact, Renew. Sustain. Energy Rev. 50 (2015) 445–456, https://doi.org/10.1016/j.rser.2015.05.035.
[8] L.W. Wang, R.Z. Wang, R.G. Oliveira, A review on adsorption working pairs for refrigeration, Renew. Sustain. Energy Rev. 13 (2009) 518–534, https://doi.org/10.1016/j.rser.2007.12.002.
[9] I.S. Glaznev, Y.I. Aristov, Kinetics of water adsorption on loose grains of SWS-1L under isobaric stages of adsorption heat pumps: the effect of residual air, Int. J. Heat Mass Transf. 51 (2008) 5823–5827, https://doi.org/10.1016/j.ijheatmasstransfer.2008.04.061.
[10] B. Dawoud, On the effect of grain size on the kinetics of water vapor adsorption and desorption into/from loose pellets of FAM-Z02 under a typical operating condition of adsorption heat pumps, J. Chem. Eng. Jpn. 40 (2007) 1298–1306, https://doi.org/10.1252/jcej.07WE163.
[11] B. Dawoud, Y. Aristov, Experimental study on the kinetics of water vapor sorption on selective water sorbents, silica gel and alumina under typical operating conditions of sorption heat pumps, Int. J. Heat Mass Transf. 46 (2003) 273–281, https://doi.org/10.1016/S0017-9310(02)00288-0.
[12] R.H. Mohammed, O. Mesalhy, M.L. Elsayed, S. Hou, M. Su, L.C. Chow, Physical properties and adsorption kinetics of silica-gel/water for adsorption chillers, Appl. Therm. Eng. 137 (2018) 368–376, https://doi.org/10.1016/j.applthermaleng.2018.03.088.
[13] L. Schnabel, M. Tatlier, F. Schmidt, A. Erdem-Şenatalar, Adsorption kinetics of zeolite coatings directly crystallized on metal supports for heat pump applications (adsorption kinetics of zeolite coatings), Appl. Therm. Eng. 30 (2010) 1409–1416, https://doi.org/10.1016/j.applthermaleng.2010.02.030.
[14] M. Mikhaeil, M. Gaderer, B. Dawoud, On the development of an innovative adsorber plate heat exchanger for adsorption heat transformation processes; an experimental and numerical study, Energy 207 (2020), https://doi.org/10.1016/j.energy.2020.118272.
[15] M. Mikhaeil, M. Gaderer, B. Dawoud, Experimental Investigation of the Adsorption and Desorption Kinetics on an Open-Structured Asymmetric Plate Heat Exchanger; Matching Between Small-Scale and Full-Scale Results, Front Energy Res. 10 2022. Doi:10.3389/fenrg.2022.818486.
[16] K.C.A. Alam, B.B. Saha, Y.T. Kang, A. Akisawa, T. Kashiwagi, Heat exchanger design effect on the system performance of silica gel adsorption refrigeration systems, Int. J. Heat Mass Transf. 43 (2000) 4419–4431, https://doi.org/10.1016/S0017-9310(00)00072-7.
[17] S.W. Hong, O.K. Kwon, J.D. Chung, Application of an embossed plate heat exchanger to adsorption chiller, Int. J. Refrig. 65 (2016), https://doi.org/10.1016/j.ijrefrig.2016.02.012.
[18] M. Mahdavikhah, H. Niazmand, Effects of plate finned heat exchanger parameters on the adsorption chiller performance, Appl. Therm. Eng. 50 (2013) 939–949, https://doi.org/10.1016/j.applthermaleng.2012.08.033.
[19] A. Sapienza, S. Santamaria, A. Frazzica, A. Freni, Influence of the management strategy and operating conditions on the performance of an adsorption chiller, Energy 36 (2011) 5532–5538, https://doi.org/10.1016/j.energy.2011.07.020.
[20] S.K. Yeboah, J. Darkwa, A critical review of thermal enhancement of packed beds for water vapour adsorption, Renew. Sustain. Energy Rev. 58 (2016) 1500–1520, https://doi.org/10.1016/j.rser.2015.12.134.
[21] S. Zhang, X. Niu, Y. Li, G. Chen, X. Xu, Numerical simulation and experimental research on heat transfer and flow resistance characteristics of asymmetric plate heat exchangers, Frontiers in Energy. 14 (2020) 267–282, https://doi.org/10.1007/s11708-020-0662-7.
[22] R. Eldeeb, V. Aute, R. Radermacher, A survey of correlations for heat transfer and pressure drop for evaporation and condensation in plate heat exchangers, Int. J. Refrig. 65 (2016) 12–26, https://doi.org/10.1016/j.ijrefrig.2015.11.013.
[23] Z.H. Ayub, T.S. Khan, S. Salam, K. Nawaz, A.H. Ayub, M.S. Khan, Literature survey and a universal evaporation correlation for plate type heat exchangers, Int. J. Refrig. 99 (2019) 408–418, https://doi.org/10.1016/j.ijrefrig.2018.09.008.
[24] M. Imran, M. Usman, Y. Yang, B.-S. Park, Flow boiling of R245fa in the brazed plate heat exchanger: Thermal and hydraulic performance assessment, Int. J. Heat Mass Transf. 110 (2017) 657–670, https://doi.org/10.1016/j.ijheatmasstransfer.2017.03.070.
[25] J.R. García-Cascales, F. Vera-García, J.M. Corberán-Salvador, J. Gonzálvez-Maciá, Assessment of boiling and condensation heat transfer correlations in the modelling of plate heat exchangers, Int. J. Refrig 30 (2007) 1029–1041, https://doi.org/10.1016/j.ijrefrig.2007.01.004.
[26] A. Jokar, M.H. Hosni, S.J. Eckels, Dimensional analysis on the evaporation and condensation of refrigerant R-134a in minichannel plate heat exchangers, Appl. Therm. Eng. 26 (2006) 2287–2300, https://doi.org/10.1016/j.applthermaleng.2006.03.015.
[27] E. Lee, H. Kang, Y. Kim, Flow boiling heat transfer and pressure drop of water in a plate heat exchanger with corrugated channels at low mass flux conditions, Int. J. Heat Mass Transf. 77 (2014) 37–45, https://doi.org/10.1016/j.ijheatmasstransfer.2014.05.019.
[28] V. Palomba, A. Frazzica, Experimental study of a fin-and-tube heat exchanger working as evaporator in subatmospheric conditions, Appl. Therm. Eng. 175 (2020), 115336, https://doi.org/10.1016/j.applthermaleng.2020.115336.
[29] P.C. Thimmaiah, A. Sharafian, M. Rouhani, W. Huttema, M. Bahrami, Evaluation of low-pressure flooded evaporator performance for adsorption chillers, Energy 122 (2017) 144–158, https://doi.org/10.1016/j.energy.2017.01.085.
[30] F. Lanzerath, J. Seiler, M. Erdogan, H. Schreiber, M. Steinhilber, A. Bardow, The impact of filling level resolved: Capillary-assisted evaporation of water for adsorption heat pumps, Appl. Therm. Eng. 102 (2016) 513–519, https://doi.org/10.1016/j.applthermaleng.2016.03.052.

[31] J. Seiler, F. Lanzerath, C. Jansen, A. Bardow, Only a wet tube is a good tube: understanding capillary-assisted thin-film evaporation of water for adsorption chillers, Appl. Therm. Eng. 147 (2019) 571–578, https://doi.org/10.1016/j.applthermaleng.2018.08.024.
[32] F. Giraud, C. Toublanc, R. Rullière, J. Bonjour, M. Clausse, Experimental study of water vaporization occurring inside a channel of a smooth plate-type heat exchanger at subatmospheric pressure, Appl. Therm. Eng. 106 (2016) 180–191, https://doi.org/10.1016/j.applthermaleng.2016.05.151.
[33] F. Giraud, P. Vallon, B. Tremeac, Experimental study of water vaporization occurring inside the channel of a smooth-plate type heat exchanger connected to an adsorber and comparison with trends observed in absorption configuration, Int. J. Refrig 77 (2017) 60–74, https://doi.org/10.1016/j.ijrefrig.2017.02.021.
[34] R. Volmer, J. Eckert, G. Füldner, L. Schnabel, Evaporator development for adsorption heat transformation devices – Influencing factors on non-stationary evaporation with tube-fin heat exchangers at sub-atmospheric pressure, Renew. Energy 110 (2017) 141–153, https://doi.org/10.1016/j.renene.2016.08.030.
[35] Marcello Masgrau, Plate for a heat exchanger and a heat exchanger, Wo-2015/057115 A1, 2015.
[36] https://www.alfalaval.com/contentassets/11dca8962e464b58932c125e47fa8eeb/gl50—gln50_product-leaflet.pdf.
[37] M. Mikhaeil, M. Gaderer, B. Dawoud, Experimental investigation of the adsorption and desorption kinetics in a closed-structured asymmetric plate heat exchanger; matching between small-scale and full-scale results, in: The 6th International Symposium on Innovative Materials and Processes in Energy Systems, IMPRES 2022, 25th – 28th October 2022, Barcelona, Spain.
[38] M. Mikhaeil, M. Gaderer, B. Dawoud, On the effect of the adsorber plate heat exchanger size on the adsorption dynamics of a thermally driven intermittent adsorption unit, in: The 6th International Symposium on Innovative Materials and Processes in Energy Systems, IMPRES 2022, 25th – 28th October 2022, Barcelona, Spain.
[39] M. Mikhaeil, M. Gaderer, B. Dawoud, A comparative experimental study on the dynamic performance of two different adsorber plate heat exchangers for adsorption energy transformation processes, in: The 6th International Symposium on Innovative Materials and Processes in Energy Systems, IMPRES 2022, 25th – 28th October 2022, Barcelona, Spain.
[40] KERN & Sohn GmbH, "Betriebsanleitung Präzisionswaagen," Manual, 2016.ttps://dok.kern-sohn.com/manuals/files/German/EMB-BA-d-1636.pdf.
[41] P. Vacuum, CMR 362, 100 hPa F.S., DN 16 ISO-KF, Manual (2019). https://www.pfeiffer-vacuum.com/productPdfs/PTR24611.en.pdf.
[42] A.G. Siemens, Katalogauszug SITRANS F M MAG 5000, SITRANS F M MAG 6000, Manual (2020). file:///C:/Users/SEBAST~1/AppData/Local/Temp/sitransf_fmmag50006000_fi01_de.pdf.
[43] Temperatur Messelemente Hettstedt Gmbh, "TMH GmbH Katalog," Manual, 2020. https://www.temperaturmesstechnik.de/fileadmin/user_upload/pdf/tmh-katalog.pdf.
[44] A. Sapienza, A. Velte, I. Girnik, A. Frazzica, G. Füldner, L. Schnabel, Y. Aristov, "Water - Silica Siogel" working pair for adsorption chillers: adsorption equilibrium and dynamics, Renew Energy 110 (2017) 40–46, https://doi.org/10.1016/j.renene.2016.09.065.
[45] V. Gnielinski, G4 Heat Transfer in Flow Past a Plane Wall, in: VDI Heat Atlas, Springer Berlin Heidelberg, Berlin, Heidelberg, 2010: pp. 713–716. Doi:10.1007/978-3-540-77877-6_37.
[46] J. Turnow, N. Kornev, V. Zhdanov, E. Hassel, Flow structures and heat transfer on dimples in a staggered arrangement, Int. J. Heat Fluid Flow 35 (2012) 168–175, https://doi.org/10.1016/j.ijheatfluidflow.2012.01.002.
[47] N.K. Burgess, P.M. Ligrani, Effects Of dimple depth on channel nusselt numbers and friction factors, J. Heat Transfer 127 (2005) 839–847, https://doi.org/10.1115/1.1994880.
[48] Y. Rao, B. Li, Y. Feng, Heat transfer of turbulent flow over surfaces with spherical dimples and teardrop dimples, Exp. Therm Fluid Sci. 61 (2015) 201–209, https://doi.org/10.1016/j.expthermflusci.2014.10.030.
[49] R. Lang, Leistungsfähige Adsorptionsmodule für eine Zeolith-Wasser-Adsorptionswärmepumpe, PhD-Dissertation, RWTH-Aachen University, Shaker Verlag GmbH, Aachen, Germany, 1994.
[50] T. Westterfeld, Numerische Untersuchung einer periodisch arbeitenden Adsorptionswärmepumpe, RWTH-Aachen University, Shaker Verlag GmbH, Aachen, Germany, 1996. PhD-Dissertation,.
[51] Y. Sato, B. Niceno, Pool boiling simulation using an interface tracking method: From nucleate boiling to film boiling regime through critical heat flux, Int. J. Heat Mass Transf. 125 (2018) 876–890, https://doi.org/10.1016/j.ijheatmasstransfer.2018.04.131.
[52] M. Ishii, T. Hibiki, Thermo-fluid dynamics of two-phase flow, springer, New York, New York, NY (2011), https://doi.org/10.1007/978-1-4419-7985-8.
[53] V.K. Dhir, Nucleate Pool Boiling, in: Handbook of Thermal Science and Engineering, Springer International Publishing, Cham, 2017: pp. 1–50. Doi: 10.1007/978-3-319-32003-8_41-1.
[54] K.L. Wolf, Physik und Chemie der Grenzflächen, Springer, Berlin Heidelberg, Berlin, Heidelberg (1957), https://doi.org/10.1007/978-3-642-49700-1.
[55] A. Horsthemke, Die Benetzung metallischer Oberflächen durch Wasser, PhD-Dissertation, Technical University of Hannover, 1980.
[56] W.A. Zisman, Influence of constitution On adhesion, Ind. Eng. Chem. 55 (1963) 18–38, https://doi.org/10.1021/ie50646a003.
[57] Z.I. Harmati, Vergleichende Untersuchungen über die Benetzung metallischer Werkstoffe gegenüber wässrigen Elektrolytlösungen unter besonderer Berücksichtigung des Korrosionsverhaltens, PhD-Dissertation, ETH Zürich, switzerland, 1980.
[58] A.W. Adamson, A.P. Gast, Physical chemistry of surfaces, Interscience, New York, 1967.
[59] J.J. Bikerman, Physical surfaces, Academic Press, New York, 1970.
[60] T. Hobler, J. Czajka, Minimum wetting rate of a flat surface, Chemia Stosow. 2B (1968) 169–186.
[61] J. Monteith, M. Unsworth, Principles of environmental physics, 3rd ed., Academic Press, 2007.
[62] A. Sakoda, M. Suzuki, Fundamental study on solar powered adsorption cooling system, J. Chem. Eng. Jpn. 17 (1984) 52–57, https://doi.org/10.1252/jcej.17.52.
[63] D.B. Riffel, U. Wittstadt, F.P. Schmidt, T. Núñez, F.A. Belo, A.P.F. Leite, F. Ziegler, Transient modeling of an adsorber using finned-tube heat exchanger, Int. J. Heat Mass Transf. 53 (2010) 1473–1482, https://doi.org/10.1016/j.ijheatmasstransfer.2009.12.001.
[64] M.M. Dubinin, Progress in surface and membrane science, Academic Press, New York, 1975.
[65] P. Cheppudira Thimmaiah, A. Sharafian, W. Huttema, C. McCague, M. Bahrami, Effects of capillary-assisted tubes with different fin geometries on the performance of a low-operating pressure evaporator for adsorption cooling system applications, Appl. Energy 171 (2016) 256–265, https://doi.org/10.1016/j.apenergy.2016.03.070.
[66] K. Montazeri, H. Lee, Y. Won, Microscopic analysis of thin-film evaporation on spherical pore surfaces, Int. J. Heat Mass Transf. 122 (2018) 59–68, https://doi.org/10.1016/j.ijheatmasstransfer.2018.01.002.